A forward energy flux at submesoscales driven by frontogenesis

Kaushik Srinivasan[a] , Roy Barkan[b,a] and James C. McWilliams[a]

[a] *Department of Atmospheric and Oceanic Sciences, University of California, Los Angeles, California, USA*

[b] *Porter School of the Environment and Earth Sciences, Tel Aviv University, Tel Aviv, Israel*

Corresponding author: Kaushik Srinivasan, kaushiks@atmos.ucla.edu

ABSTRACT: Submesoscale currents, comprising fronts and mixed-layer eddies, exhibit a dual cascade of kinetic energy: a forward cascade to dissipation scales at fronts and an inverse cascade from mixed-layer eddies to mesoscale eddies. Within a coarse-graining framework using both spatial and temporal filters, we show that this dual cascade can be captured in simple mathematical form obtained by writing the cross-scale energy flux in the local principal strain coordinate system, wherein the flux reduces to the the sum of two terms, one proportional to the convergence and the other proportional to the strain. The strain term is found to cause the inverse energy flux to larger scales while an approximate equipartition of the convergent and strain terms capture the forward energy flux, demonstrated through model-based analysis and asymptotic theory. A consequence of this equipartition is that the frontal forward energy flux is simply proportional to the frontal convergence. In a recent study, it was shown that the Lagrangian rate of change of quantities like the divergence, vorticity and horizontal buoyancy gradient are proportional to convergence at fronts implying that horizontal convergence drives frontogenesis. We show that these two results imply that the primary mechanism for the forward energy flux at fronts is frontogenesis. We also analyze the energy flux through a Helmholtz decomposition and show that the rotational components are primarily responsible for the inverse cascade while a mix of the divergent and rotational components cause the forward cascade, consistent with our asymptotic analysis based on the principal strain framework.

1. Introduction

Most of the kinetic energy (KE) in the earth's oceans is found in mesoscale eddies consequent of which, understanding the mechanisms and pathways of their generation and dissipation is of fundamental importance (Ferrari and Wunsch 2009). Since they are approximately in geostrophic balance, classical geostrophic turbulence theory (Salmon 1998) provides a paradigm wherein available potential energy (APE) created by the action of large scale wind stress and surface buoyancy fluxes is converted into kinetic energy through baroclinic instability. Nonlinear eddy-eddy interactions then induce an inverse cascade of this kinetic energy to larger eddy scales, with their dissipation primarily limited to occur at the boundaries, both at the ocean bottom and, as has been demostrated recently, the air-sea interface (Ma et al. 2016; Renault et al. 2016, 2018, 2019; Rai et al. 2021). Studies over the past two decades have, however, found that mesoscale eddies can have significant energy exchanges with smaller and faster oceanic components comprising submesocale mixed layer eddies (MLEs) and fronts (Thomas et al. 2008; McWilliams 2016), and inertia gravity waves (IGWs) (Thomas 2012; Xie and Vanneste 2015; Taylor and Straub 2016; Alford et al. 2016; Jing et al. 2017; Barkan et al. 2017; Rocha et al. 2018; Thomas and Daniel 2021; Barkan et al. 2021). Mesoscale eddies have horizontal length scales in the range O(10km-100km) and time scales of weeks to a months. MLEs typically have O(1-10km) while cross-frontal scales can be as small as tens of metres. While MLEs can last a few days, frontal time scales can overlap with those of IGWs that are physically constrained to be faster than the local Coriolis frequency.

Like mesoscale eddies, MLEs are also formed through baroclinic instability but of the near-surface mixed layer (Boccaletti et al. 2007), which is deeper during the winter season due to surface cooling driven convective mixing (Mensa et al. 2013; Brannigan et al. 2015; Callies et al. 2015; Thompson et al. 2016). In fact layered quasi-geostrophic models that have been a long standing framework for studying mesoscale eddies also reproduce MLEs with a shallow upper layer, but not fronts (Callies et al. 2016). Fronts, which are highly anisotropic structures, are formed through a multitude of mechanisms (Hoskins and Bretherton 1972; McWilliams 2017; Srinivasan et al. 2017) that involve the background gradients provided by both mesoscale eddies and MLEs, but also the turbulence in the mixed layer (McWilliams et al. 2015; Wenegrat and McPhaden 2016; McWilliams 2017). Energetically, the generation of both fronts and MLEs involves a conversion of mixed layer APE to KE, but unlike MLEs, fronts also have a significant ageostrophic flow component in the

cross-front direction i.e. the ageostrophic secondary circulation (ASC). Frontal ASCs are highly asymmetric, with strong downwelling and weak upwelling, and this manifests as a large visible negative value of the divergence in the mixed layer, $\delta = u_x + v_y$ (u and v are the velocities along the zonal, x, and meridional, y, directions). Heuristically one might expect that the similarity in the generation and balance of mesoscale eddies and MLEs might lead to similar nonlinear dynamics. A recent study by Schubert et al. (2020) employed a coarse graining approach (Aluie et al. 2018) to explicitly demonstrate that MLEs undergo an inverse energy cascade to mesoscales, echoing the inverse energy transfer of mesoscale eddies themselves to larger scales. In particular they were able to provide a visual and dynamical demonstration of the absorption of MLEs into mesoscale eddies. They also show that the energy transfer at smaller scales occurs primarily at frontal features and is forward i.e. from large to small scales. This is consistent with previous studies that suggest that ageostrophic motions might be responsible for forward energy cascades found at submesoscales (Capet et al. 2008).

In this study we examine the cross scale flux of kinetic energy in realistic submesoscale resolving numerical simulations of the North Atlantic. Instead of the traditionally used spectral energy flux approach (Scott and Wang 2005; Scott and Arbic 2007; Capet et al. 2008; Molemaker et al. 2010; Barkan et al. 2015; Wang et al. 2019; Ajayi et al. 2021), we employ the filter-based coarse graining framework to compute energy fluxes across both spatial (Aluie et al. 2018; Srinivasan et al. 2019; Schubert et al. 2020) and temporal (Barkan et al. 2017, 2021; Garabato et al. 2021; Zhang et al. 2021b,a) scales. Figure 1 shows the spatial structure of the spatial KE flux from our 500 m horizontal resolution run (details in Section 2) for a filter-scale of 4km (Π^4_h, representing the horizontal KE transfer from scales larger than 4km to those smaller) during the month of January. Echoing the results of Schubert et al. (2020), we find that the flux is largest at the frontal features which can be identified as regions of strong convergence ($-\delta$) and buoyancy gradient, $|\nabla b|$. Furthermore, while some of the regions of strong forward transfer are clearly at fronts that lie on the edges of large mesoscale anticyclones (leading to the possibility that these are generated through strain-induced frontogenesis) most other regions are at fronts associated with smaller scale eddies or sometimes none at all. This indicates that the mechanism of energy flux at fronts is agnostic to the mechanism of frontal generation. The choice of 4km filter-scale in Fig. 1 is not specific and represents a typical length scale in the submesoscale range (in Sec 4a we show that

this actually corresponds to an equivalent spectral length scale of $\lambda_{sp} = 9.6$ km). In the rest of the paper, we employ a wide range of filter-scales for analysis starting from the grid scale till beyond mesoscale eddy length scales.

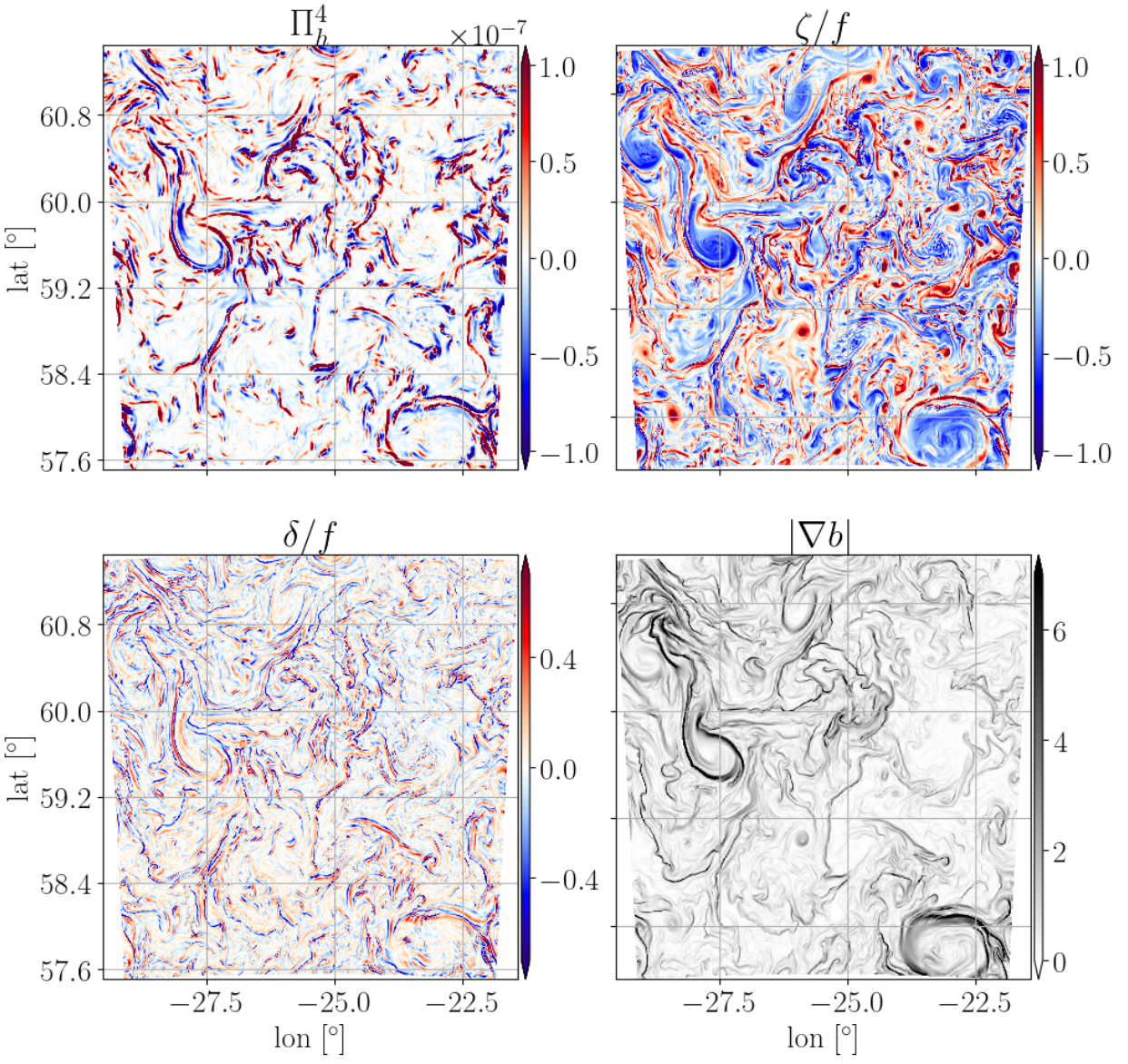

FIG. 1. A snapshot of horizontal cross-scale energy flux Π_h^4 [$m^2 s^{-3}$] on January 7th (i.e. the winter season), where the superscript indicates a filterscale of 4 km, the energy transferred from scales larger than 4 km to finer scales at a ocean surface [Note that this is equivalent to an effective spectral scale, λ_{sp} = 9.6 km (see Section 4a)]. Also shown are the surface vorticity [s^{-1}], $\zeta = v_x - u_y$ and the divergence [s^{-1}], $\delta = u_x + v_y$ normalized with the Coriolis paramter, f and the magnitude of the horizontal buoyancy gradient, $|\nabla b|$ [s^{-2}].

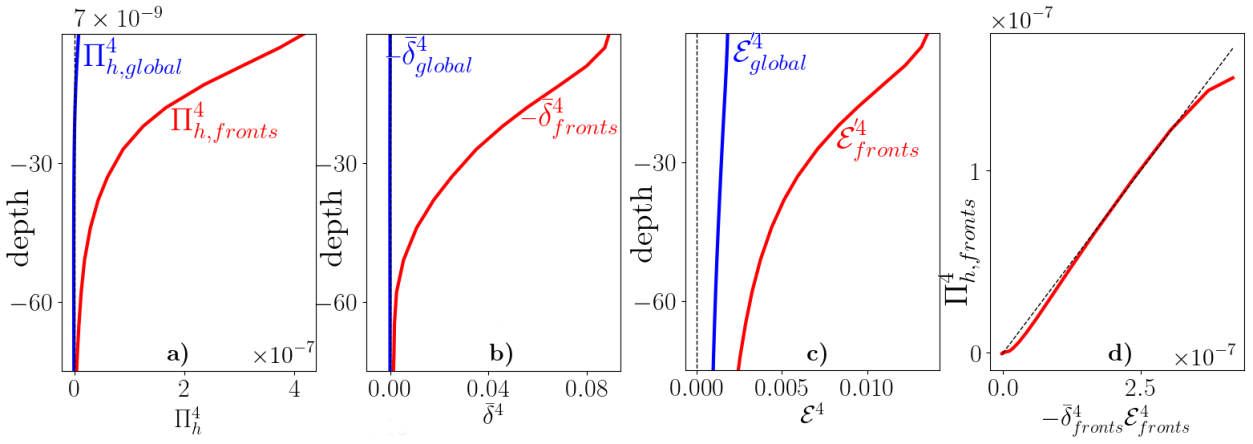

FIG. 2. Plots, as a function of depth [m], of (a) Π^4_h [m^2s^{-3}], the horizontal energy flux from scales larger than 4km to smaller scales, (b) $-\bar{\delta}^4$ [s^{-1}], the convergence smoothed at a 4km scale and, (c) $\mathcal{E}'^4$ [m^2s^{-2}], the kinetic energy of scales finer than 4 km, either spatially averaged over the entire flow domain shown in Fig. 1 (marked by the subscript, 'global' and in blue) or spatially averaged only on fronts defined by the region having $|\nabla b| > 1.5\times10^{-7}s^{-2}$ (marked by the subscript, 'fronts' and in red); temporal averaging is also performed over the winter months of January, February and March on top of the indicated spatial averaging. (d) A plot of $\Pi^4_{h,fronts}$ in a) versus $-\bar{\delta}^4_{fronts}\mathcal{E}'^4_{fronts}$ [the product of b) and c)].

To make the association between fronts and the energy flux stronger and foreshadow the results in our paper ahead, we compare the energy flux across the 4 km scale (Π^4_h) averaged over the flow domain seen in Fig. 1 with that conditionally averaged on fronts only (given by the region satisfying $\nabla b > 1.5\times10^{-7}s^{-2}$) as a function of depth (Fig. 2a). We note that both the frontal-averaged flux (red curve) and the domain-averaged flux (blue curve) are positive over this depth, i.e. a positive energy flux from scales larger than 4km to smaller or equivalently a *forward* flux. The front-averaged forward flux is also two orders of magnitude larger, supporting the visual inference from Fig. 1 that the energy flux at this scale is predominantly at fronts. The vertical structure of the front-averaged flux closely resembles that of the front-averaged convergence, $-\bar{\delta}^4_{fronts}$ (where $\bar{\delta}^4$ is the divergence smoothed at the same 4 km scale for consistency) and the kinetic energy at scales smaller than 4 km, $\mathcal{E}'^4$, averaged at fronts, $\mathcal{E}'^4_{fronts}$. It should be noted that the rate of change of $\mathcal{E}'^4$ due to the energy exchange with larger scales is precisely, Π^4_h, i.e.

$$\left(\frac{D\mathcal{E}'^4}{Dt}\right)_{transfer} = \Pi^4_h . \tag{1}$$

By plotting the $\Pi^4_{h,fronts}$ against $-\bar{\delta}^4_{fronts}\mathcal{E}'^4_{fronts}$ (a natural choice, given that the two quantities have identical dimensions) we find the simple result that the relationship is *linear*, so that $\Pi^4_h \propto -\bar{\delta}^4_{fronts}\mathcal{E}'^4_{fronts}$. But from (1) we get

$$\frac{1}{\mathcal{E}'^4_{fronts}}\left(\frac{D\mathcal{E}'^4}{Dt}\right)_{transfer,fronts} \propto -\bar{\delta}^4_{fronts}\,. \tag{2}$$

The results above can be summarized as follows: the rate of change of kinetic energy(the energy flux) at around 4km scales during the winter season in this region is predominantly at fronts while the *relative* rate of change of frontal kinetic energy is simply governed by the convergence as give by (2).

The entire analysis above was based on a combination of dimensional considerations and simple model-based heurestics, but is a key result of this study. We show that (2) can in fact be derived from first principles by writing the energy flux in principal strain coordinates (Section 3) followed by a combination of detailed model-based analysis (Section 4, including an analysis of the energy flux using the Helmholtz decomposition in Section 4c) and asymptotic theory (Section 5). Section 5 connects the results here with the theory of frontogenesis proposed by Barkan et al. (2019) demonstrating that convergence drives frontogenesis, a result that we show here also applies to the cross-scale energy flux through the form of (2). In this paper we do not explore the seasonality of the forward and inverse energy cascades as has been suggested in recent work (Garabato et al. 2021) that analyses temporal energy transfers from observational data (in particular the OSMOSIS current meter array) and find an inverse energy cascade in winter from submesoscales to mesoscales but a forward energy transfer in late spring. We instead limit our attention to the winter season in the North Atlantic when the submesoscales are strongest and examine the cross-scale KE fluxes and their structure at submesoscale spatial and temporal scales. We also briefly discuss a potentially alternative pathway for forward energy cascade, namely symmetric instability accompanied by some analysis and discussions involving the vertical component of the energy flux, Π^ℓ_v, and the corresponding geostrophic shear production, Π^ℓ_{vg} (Section 6b). In concurrent (Barkan et al. 2021) and upcoming studies we also examine the energy exchanges between eddies, fronts and IGWs.

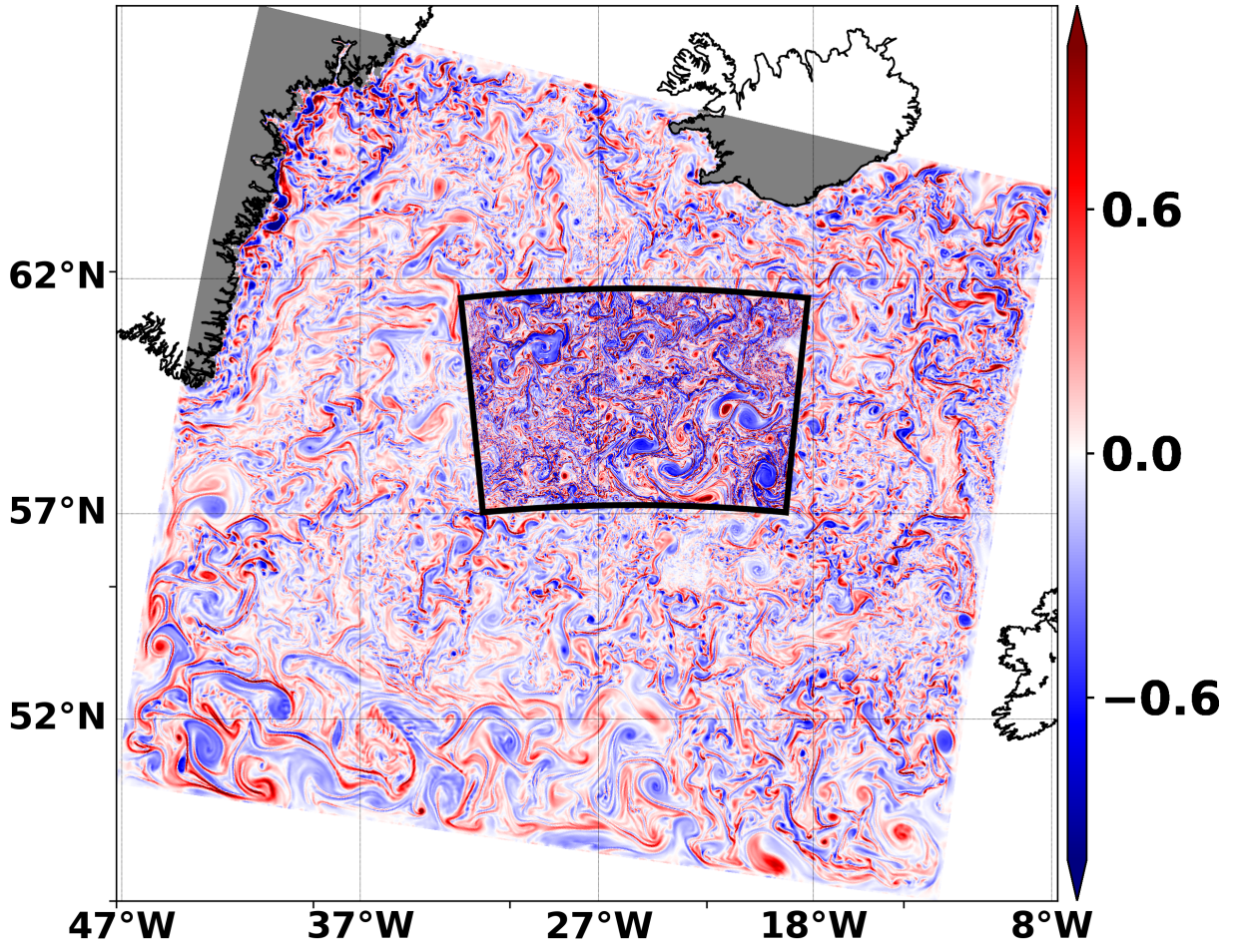

FIG. 3. A snapshot of the normalized surface vorticity, ζ/f, on February 8, obtained from the 2 km (outer nest) and 500 m (inner nest) horizontal resolution nested ROMS simulations. The 2km run, forced by a 6 km resolution North Atlantic run (not shown here), spans the North Atlantic region between Greenland and Iceland. The actual analysis region (shown in Fig. 1) for the 2 km and 500 m runs in this work is a square region spanning about two-thirds of the inner 500 m nest here.

2. Numerical methodology

Numerical solutions are conducted using the Regional Ocean Modeling System (ROMS) a split-explicit hydrostatic primitive model (Shchepetkin and McWilliams 2005). A nested grid hierarchy with one-way nesting is employed; a 6km resolution parent grid run forced on its external boundaries by climatology is run beginning 1 January, 1999 for two years with only the third year run used to force a 2 km run at the boundaries; the 2 km run is then subsequently used to

force and run a submesoscale-permitting 500 m resolution run. A surface vorticity snapshot in early February is plotted in Fig. 3 highlighting the 2 km-500 m nested hierarchy and the stronger submesoscale field of the 500 m resolution model. The actual analysis domain employed in this work is an approximately 430 km $\times$ 430 km region within the 500 m nested grid, displayed in Fig. 1. The air-sea interface is forced with the Climate Forecast System Reanalysis (CFSR) atmospheric product low pass filtered using a one-day filter to eliminate high frequency forcing that would generate Near-inertial internal waves (NIWs). We only use the winter months (January, February and March 2001) of the 500 m and 2 km runs for analysis in this study since these are the months when submesoscale MLEs and fronts are especially active. The solutions used for analysis in this paper have been validated extensively in our concurrent study (Barkan et al. 2021) against satellite altimetry and current meter observations in the region so we refer the readers to that paper.

3. Dynamics in principal strain coordinates

We compute the energy flux across scales using the so-called coarse graining approach which entails a method for decomposing the flow field into small and large scales for spatial transfers (Eyink and Aluie 2009; Aluie et al. 2018), and fast and slow scales for temporal transfers (Barkan et al. 2017). These are accomplished using a simple low-pass filtering (or smoothing) operator. In this study we separately compute cross-scale transfers across spatial and temporal scales rather than a joint spatio-temporal approach. While previous studies have been limited to computing either spatial (Aluie et al. 2018; Schubert et al. 2020) or temporal scale-to-scale transfers (Barkan et al. 2017, 2021), we compute both to demonstrate the robustness of our analysis framework. Furthermore, in the abscence of IGWs (which is true for the simulations employed here) slower (faster) scales correspond to larger (smaller) ones and this should be reflected in the cross-scale energy fluxes.

a. Scale-to-scale energy flux

We decompose the velocity fields into scales smaller (faster) and larger (slower) than a given length scale ℓ (time scale τ) with a low-pass filtering function; this is chosen to be a uniform filter (also referred to as a boxcar or tophat filter) for the spatial filtering (Aluie et al. 2018) and a Butterworth filter for the temporal (Barkan et al. 2021). The uniform filter is sharp in

physical space but the Butterworth is spectrally sharp. These filter choices and their implications are discussed in Section 4a (in particular, see the discussion around Fig. 6.). Since the theory applies to both spatial and temporal filters, we identify the slower (larger) component as $\bar{u}_i$ and the faster (smaller) component as u'_i where $i \in [1,2]$ and $(u_1, u_2) \equiv (u, v)$. In other words, because $u_i = \bar{u}^\ell + u'^\ell = \bar{u}^\tau + u'^\tau \equiv \bar{u} + u'$, we derive our expressions in general and for presentation of our results, we use τ (units in hours) superscript for the temporal transfers and ℓ (units in km) for the spatial. We call the $\bar{u}$ and u' fields as coarse and fine fields respectively. The energy transfer from scales finer than a certain scale to coarser scales is then (Aluie et al. 2018)

$$\Pi = \underbrace{-(\tau_{uu}\bar{u}_x + \tau_{uu}(\bar{u}_y + \bar{v}_x) + \tau_{uu}\bar{v}_x)}_{\Pi_h} \underbrace{-(\tau_{uw}\bar{u}_z + \tau_{vw}\bar{v}_z)}_{\Pi_v} . \tag{3}$$

where Π_h and Π_v are the vertical and horizontal energy flux terms. The Leonard's stress term (Leonard 1975) is $\tau_{uv} = \overline{uv} - \overline{u}\,\overline{v}$, and similarliy for the other terms. Since for filters, $\overline{u'}, \overline{v'} \neq 0$ (i.e. the filter operator is not a Reynolds' operator), $\tau_{uv} \neq \overline{u'v'}$. The horizontal component can be further expressed in the form,

$$\Pi_h = -\boldsymbol{\tau} : \overline{\boldsymbol{S}} = -\begin{bmatrix} \tau_{uu} & \tau_{uv} \\ \tau_{uv} & \tau_{vv} \end{bmatrix} \begin{bmatrix} \bar{u}_x & (\bar{u}_y + \bar{v}_x)/2 \\ (\bar{u}_y + \bar{v}_x)/2 & \bar{v}_y, \end{bmatrix} \tag{4}$$

where the : operator represents a tensor dot product operation (a term-by-term product followed by summation).The expression in (4) can be identified as "the stress of the finer scales times the strain of the coarser scale".

We rotate our (x, y) coordinate axis along the vertical by angle $\theta(x, y)$ at every point in space, such that in the new local coordinate system, the strain tensor, $\bar{S}_{ij}$, is diagonal. Such a $\theta(x, y)$ always exists because $\bar{S}_{ij}$ is a symmetric tensor. It is straightforward to show that that the precise form this diagonal tensor takes is

$$[\bar{S}] = \begin{bmatrix} (\bar{\delta} + \bar{\alpha})/2 & 0 \\ 0 & (\bar{\delta} - \bar{\alpha})/2 \end{bmatrix} \tag{5}$$

Where the coarse-scale divergence, $\bar{\delta} = \bar{u}_x + \bar{v}_y$ and the strain magnitude, $\bar{\alpha}^2 = (\bar{v}_y - \bar{u}_x)^2 + (\bar{v}_x + \bar{u}_y)^2$ are both quantities that are invariant to a rotation of coordinate system and can be effectively treated as scalars. Clearly, in the limit of $\bar{\delta} \to 0$, the diagonal terms reduce to $\pm\bar{\alpha}/2$, so that the latter can also be referred to as the "non-divergent" strain though we drop the characterization in our usage here. In this rotated coordinate system the energy flux takes the form

$$\Pi_h = -[\tau_{uu}(\bar{\delta} + \bar{\alpha})/2 + \tau_{vv}(\bar{\delta} - \bar{\alpha})/2], \tag{6}$$

$$= (\tau_{vv} - \tau_{uu})\frac{\bar{\alpha}}{2} - (\tau_{vv} + \tau_{uu})\frac{\bar{\delta}}{2}, \tag{7}$$

$$= \underbrace{\mathcal{E}'\gamma\bar{\alpha}}_{\Pi_\alpha} - \underbrace{\mathcal{E}'\bar{\delta}}_{-\Pi_\delta}. \tag{8}$$

where $\mathcal{E}' = (\tau_{vv} + \tau_{uu})/2$ is the energy of finer scales, and $\bar{\delta}$ and $\bar{\alpha}$ are the divergence and strain of the coarse field. The parameter

$$\gamma \equiv \frac{\tau_{vv} - \tau_{uu}}{\tau_{vv} + \tau_{uu}} \tag{9}$$

is the anisotropy of finer scales in principal strain coordinates (Huang and Robinson 1998; Srinivasan and Young 2014). It is important to emphasize the coordinate system when discussing γ because unlike $\bar{\alpha}$, $\bar{\delta}$ and $\mathcal{E}'$, γ is not invariant to rotation. The term Π_α in related contexts is referred to as the deformation shear production (DSP) (Thomas 2012) but the Π_δ is new and is in general only relevant when $\bar{\delta}$ is significant i.e. for submesoscale currents and so we call it the convergence production (CP). Note that $-1 \le \gamma \le 1$ which gives the bounds $-\alpha\mathcal{E}' \le \Pi_\alpha \le \alpha\mathcal{E}'$. The expression in (8) can also be written in coordinate invariant form as

$$\Pi_h = \underbrace{(\tau_{vv} - \tau_{uu})\frac{\bar{\sigma}_n}{2} - \tau_{uv}\bar{\sigma}_s}_{\Pi_\alpha} - \underbrace{(\tau_{vv} + \tau_{uu})\frac{\bar{\delta}}{2}}_{-\Pi_\delta}, \tag{10}$$

The Π_δ expectedly remains unchanged as it is the product of two coordinate invariant quantities, $\mathcal{E}' = (\tau_{vv} + \tau_{uu})/2$ and $\bar{\delta} = \bar{u}_x + \bar{v}_y$ but the two terms comprising Π_α associated with the normal strain, $\sigma_n = \bar{u}_x - \bar{v}_y$ and shear strain, $\sigma_s = \bar{u}_y + \bar{v}_x$ are not invariant and therefore have no separate meaning. While the principal strain form of Π_α in (8) has a very simple elegant form, estimating

γ in principal strain coordinates is not straightforward and we mostly use the coordinate-free form specified in (10).

Eq. (10) with $\delta = 0$ was derived by Polzin (2010), for studying the interactions between IGWs and mesoscale flows, in straightforward fashion from (3). Even with $\delta \neq 0$, starting from (10) and showing that Π_h is equivalent to the form in (3) is easily done. However directly inferring the form of Π_h in (10) from (3) is not obvious and the principal strain coordinates helps arrive there naturally. The treatment of Π_h in principal strain coordinates outlined above follows that by Jing et al. (2017) in their study of near-inertial mesoscale eddy interactions, who derived the form in (7) for $\delta = 0$; in essense, $\Pi_h \propto \alpha$, where α is the mesoscale strain field. Our treatment extends the result to submesoscale flows for finite δ and we use it in the more general coarse-graining context.

b. Frontogenetic equations

The primary focus of this study is to examine the connection between energy transfer at fronts and frontogenesis. To this end we consider the evolution equation for the buoyancy gradient, $|\nabla b|^2 = b_x^2 + b_y^2$, also referred to as the frontogenetic tendency equation (Hoskins and Bretherton 1972),

$$\frac{1}{2}\frac{D||\nabla b||^2}{Dt} = \underbrace{-(b_x^2 u_x + b_y^2 u_y) + b_x b_y (u_y + v_x)}_{\mathcal{B}_h} \underbrace{-b_z (w_x b_x + w_y b_y)}_{\mathcal{B}_v} \tag{11}$$

Then we can write (Barkan et al. 2019)

$$\mathcal{B}_h = -\boldsymbol{B} : \boldsymbol{S}, \tag{12}$$

where $\boldsymbol{S}$ is the strain tensor while

$$\boldsymbol{B} = \begin{bmatrix} b_x^2 & b_x b_y \\ b_x b_y & b_y^2 \end{bmatrix} \tag{13}$$

is a *dyadic*, a special kind of second rank tensor formed by the outer product of two vectors, in this case of (b_x, b_y) with itself. Comparing (12) with (4) we note that the horizontal component

of the buoyancy gradient tendency can be written in the same form as the horizontal component of the fine-scale energy tendency (4), with the fine scale stress tensor, $\boldsymbol{\tau}$ replaced by the buoyancy gradient tensor $\boldsymbol{B}$. As before we switch to the principal strain coordinates, and retracing the steps from (5) to (8) for (12) we get

$$\mathcal{B}_h = (|\nabla b|^2 \gamma_b \alpha - |\nabla b|^2 \delta)/2\,. \tag{14}$$

where γ_b is the buoyancy gradient anisotropy in principal strain coordinates

$$\gamma_b \equiv \frac{b_x^2 - b_y^2}{b_x^2 + b_y^2}\,, \tag{15}$$

and the coordinate free form of (14) in analogy with (10)

$$\mathcal{B}_h = \underbrace{(b_y^2 - b_x^2)\frac{\sigma_n}{2} - b_x b_y \sigma_s}_{B_\alpha} \underbrace{- \,(b_y^2 + b_x^2)\frac{\delta}{2}}_{-B_\delta}\,. \tag{16}$$

Recently (Balwada et al. 2021) derived the evolution equations for square of the gradient of a passive scalar ($|\nabla c|^2$) in principal strain coordinates, which is essentially the same as that of $|\nabla b|^2$ derived above, although the authors do not express the result in the $\alpha - \delta$ form that we prefer or in the coordinate-free form in (16). In general, an equation like (16) can be written for any physical quantity whose rate of change takes the form in (12). Beyond scalar fields like b, we state (without elaboration) that similar forms can be written for the evolution equations of the square vertical shear, $u_z^2 + v_z^2$ [employed in the study of topographic submesoscale wakes (Srinivasan et al. 2021) and front-surface wave interactions (Hypolite et al. 2021)] and the magnitude of the velocity gradient tensor, $|\nabla \boldsymbol{u}|^2$ [used as another proxy for frontogenesis by Barkan et al. (2019)]

4. Results from the numerical model

a. Spatiotemporally averaged fluxes

We compute the fluxes Π_h, Π_α and Π_δ from (10) at multiple depth levels between 0 and 100 m for two model runs at 2 km and 500 m resolutions. For each of the two runs and at each depth we use a range of scales for computing the fluxes - the spatial filter sizes are varied between the

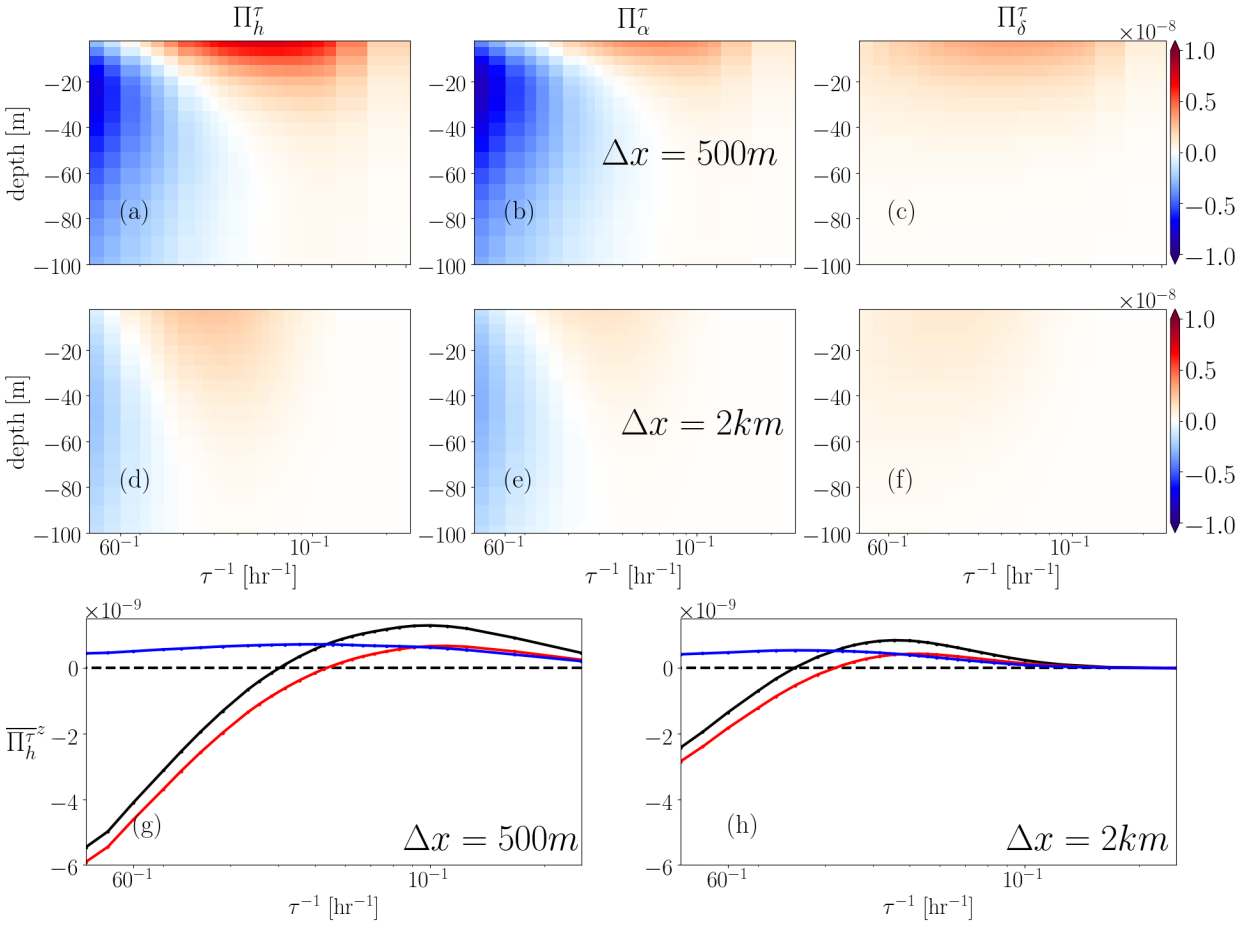

FIG. 4. Horizontally and temporally averaged temporal energy fluxes [m^{2}s^{-3}] (a)-(f) as a function of depth and inverse filterscale [hr^{-1}] and (g), (h) vertically averaged over the top 50m. The top row shows fluxes at 500 m resolution and the second row at 2 km resolution. The curves in the bottom row are the total horizontal flux Π_h^τ (black), the deformation shear production Π_α^τ(red) and the convergence production Π_δ^τ(blue).

lowest grid scale (500 m and 2 km for the two models) to around 100 km while the temporal scales are varied between 1 hr and 100 hrs. Computing the fluxes on a cluster (XSEDE (Towns et al. 2014)) using the Ray multiprocessing library [1] allows us to use a significantly larger number of filters, 54 filters in space and 27 fiters in time at a large number of depths, compared to recent studies. The coarse-graining approach has the advantage over spectral methods in not needing a windowing function for ensuring periodicity at the boundaries, but a consistent treatment of the filter at the boundaries is still required. Whenever the spatial (uniform) filter hits the boundary, we use a mirroring of the velocity field outward, preserving the structure of the flow. For the temporal

[1]https://github.com/ray-project/ray

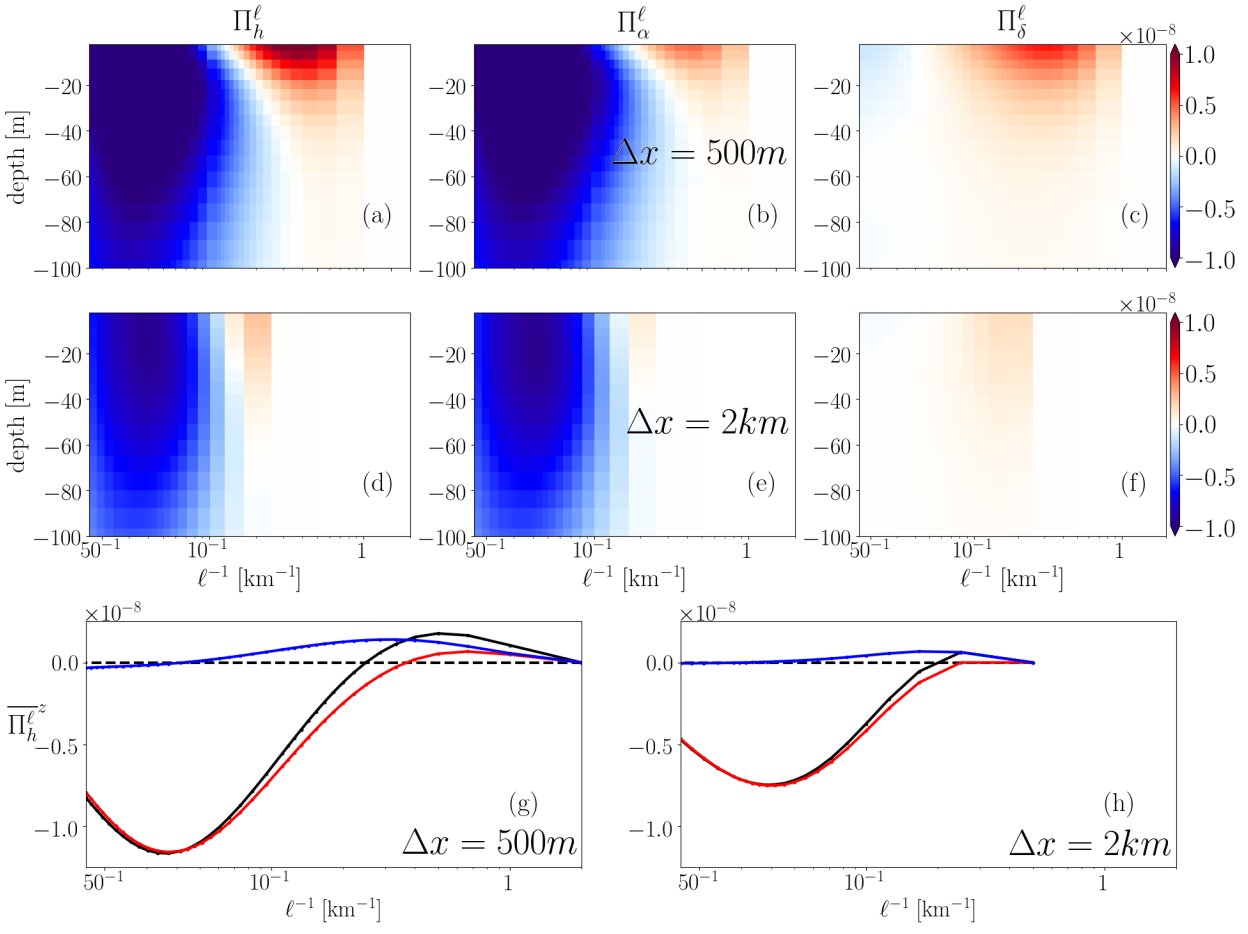

FIG. 5. Horizontally and temporally averaged spatial energy fluxes [m^{2}s^{-3}] (a)-(f) as a function of depth and inverse filterscale [km^{-1}] and (g), (h) vertically averaged over the top 50m. The top row shows fluxes at 500 m resolution and the second row at 2 km resolution. The curves in the bottom row are the total flux Π_h^ℓ (black), the deformation shear production Π_α^ℓ(red) and the convergence production Π_δ^ℓ(blue).

(Butterworth) filter, after filtering, we discared the first 120 hours (being about twice the length of the largest filter used) in January and last 120 hrs in March to avoid edge efftecs.

We first show Π_h, Π_α and Π_δ spatially averaged over the domain and temporally averaged over the winter season (sans the edge data for the temporal case) in Figs. 4a-f (temporal transfer) and 5a-f (spatial transfer). These represent the average energy transferred over the whole domain and during the winter months from scales larger to smaller. Thus positive values represent an energy transfer to smaller scales (or a forward cascade) and negative values represent an inverse energy cascade. Both figures show broadly similar patterns, in particular inverse cascade at larger (slower)

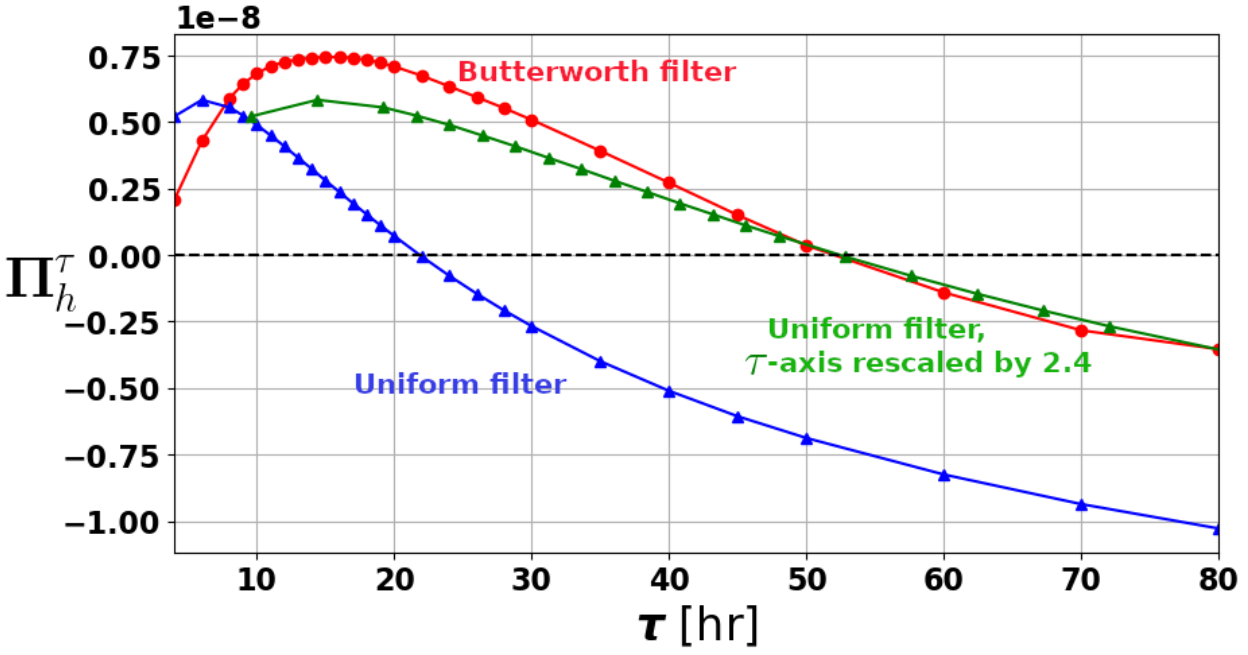

FIG. 6. Horizontally and temporally averaged temporal energy flux (Π_h^τ [m^2s^{-3}]) at the surface as a function of filterscale, τ [hr] for the choice of two filters, the Butterworth (red) and uniform (blue) filters. The green curve is simply the blue curve plotted against 2.4τ, i.e. by rescaling the abscissa by a factor of 2.4. The red curve is precisely the surface value in Fig. 4a although the abscissa here is τ instead of τ^{-1}.

scales and forward cascade at smaller (faster) scales. The transition from forward to inverse transfer is at 10km and around 50 hrs at the surface.

These transition scales need to be interpreted with some care given the different filter choices in the two cases, the spatially sharp uniform filter and the spectrally sharp Butterworth filter in time. To evaluate the importance of these filter choices on the flux, we also compute a temporal scale-to-scale flux with the uniform filter at the surface and compare it with the flux obtained using the Butterworth filter. Fig. 6 highlights the result that the forward-to-inverse transition timescale obtained from the Butterworth filter is around 2.4 times larger than what one might expect from the uniform filter flux calculation as demonstrated by plotting the flux obtained using the uniform filter against 2.4τ instead of the actual filterscale, τ. Given the lack of an obvious implementation of the Butterworth filter to two dimensions, we continue using the uniform filter, in line with recent studies (Aluie et al. 2018; Schubert et al. 2020) with the knowledge that forward cascade region in Fig. 5 occupies a larger range of scales and the actual transition scale is at a scale of 24km, rather

than 10km result found in Fig. 5. In particular, we introduce an equivalent spectral scale for the spatial flux calulations $\lambda_{sp} = 2.4\ell$ and report it along with the actual filter scale ℓ. Later, in Sec. 6a we again demonstrate the effective spectral resolution of the uniform filter, but by comparing energy spectra instead of fluxes (see Fig. 13). A similar result was found by Schubert et al. (2020) by comparing the traditional spectral flux (in space) with the result from the coarse-grained fluxes from the uniform filter as done here although they obtained a factor of 2 instead of 2.4. We surmise that this is a consequence of the larger number of filters sizes used here, making it easier for us to estimate this factor accurately.

While the temporal transition scale is around 50 hr, a majority of the forward cascade (Figs. 4a and 6) is actually found within 24hr timescales. A recent study (Ajayi et al. 2021) computed (spatial) spectral energy fluxes at different regions of the North Pacific for a 1km resolution ocean model and found that using daily averages instead of snapshots substantially suppressed the forward energy cascade signal. Our temporal flux results explicate why this might be, assuming that in the absence of waves, the scales of motion associated with the temporal forward flux correspond to those that result in the spatial forward energy flux.

Both the forward and inverse cascade are weaker in the 2 km model run consistent with the notion that the 500 m model resolves both submesoscale MLEs and fronts better. The peak inverse energy flux is at ℓ=30 km (λ_{sp} = 72 km) in the spatial though it is slower than the largest temporal filter width used here (i.e. slower than around 3 days which is still consistent with average MLE lifetimes of around a few days). In subsequent discussions we exclusively focus on the 500 m nest given the inadequecy of the 2 km nest in resolving submesoscales.

The most interesting results concern the breakup of Π_h into Π_α and Π_δ. Specifically, the inverse energy transfers in both the spatial and temporal cases are almost entirely due to the Π_α (or the DSP term); while the forward energy fluxes are approximately equipartitioned in the temporal case, the Π_δ (the CP term) is slightly larger in the spatial case. However, looking at the vertically integrated transfers, we notice that for scales smaller than 5 km (λ_{sp} = 12 km) and slower than around 10 hrs, both the Π_δ and the Π_α do in fact seem to converge, this being especially evident for the temporal case. We use the scaling for frontogenesis used in Barkan et al. (2019) to support the hypothesis that for small enough scales, there is an equipartition between Π_α and Π_δ. In general, the fact that the $\Pi_\delta = -\mathcal{E}'\delta$ is positive at the smallest, fastest scales in is line with our expectations about fronts,

whose strong near-surface convergence (i.e. negative δ) should lead to positive values for Π_δ. This also offers clear evidence for the hypothesis by Capet et al. (2008) that the forward energy cascade is due to ageostrophic motions (geostrophic flows have negligible δ). However the cause of the forward cascade contribution of Π_α are less clear. We plot the spatial and temporal energy spectra for the 2 km and 500 m winter runs (Fig. 7). Both show a larger level of energy at all scales in the 500 m model run relative to 2 km model. This is broadly consistent with the stronger inverse energy cascade in the 500 m model relative to the 2 km model from MLEs to larger scales. The 500 m model has a larger energy even at small scales in spite of having a stronger forward cascade. This is because both frontal dynamics and mixed layer instability are accompanied by a conversion of APE to KE, energizing the surface mixed layer. A quantitative explanation of the equilibrium structure of the energy spectrum would require a full spectral kinetic energy budget, which is not the focus here.

b. The spatial structure of energy fluxes

To shed greater light on the transfers, following Fig. 1, we visualize the spatial structure of Π_α and Π_δ in for different filter scales, along with the other components that constitute (8): $\bar{\alpha}$, $\bar{\delta}$, $\mathcal{E}'$ and the principal strain anisotropy in the form $\gamma\mathcal{E}' = (\tau_{vv} - \tau_{uu})/2$. For a filter scale of $\ell = 4km$ (λ_{sp} = 9.6 km) we plot this breakup in Fig. 8. An immediate observation is the close similarity of the Π_α and Π_δ fields to the extent that they almost look identical at first glance. This further lends credence to the hypothesis that at frontal spatial scales, there is an approximate equipartition between the two terms. The largest positive values in the Π_α and Π_δ fields are found in regions where $\bar{\delta}$ is strongly negative (i.e. regions of strong convergence). The small scale kinetic energy is also collocated with the convergent regions , as is the anisotropy $\gamma\mathcal{E}'$ which suggests that that these two quantities are associated with the ageostrophic secondary circulation of the fronts, whose signature is the convergent region. The large scale strain $\bar{\alpha}$ also has a distinctly frontal structure but encompasses regions of both positive and negative divergence and has a broader extent than the other fields. It is important to keep in mind that this section explains the forward energy cascades at fronts purely based on the structure of fronts themselves; this is obvious in the case Π_δ but a little more nuanced in the case of Π_α. We provide a simple theoretical framework explaining this connection between the forward cascade at fronts and frontogenesis in the Sec. 5. The correspondence between Π_α and

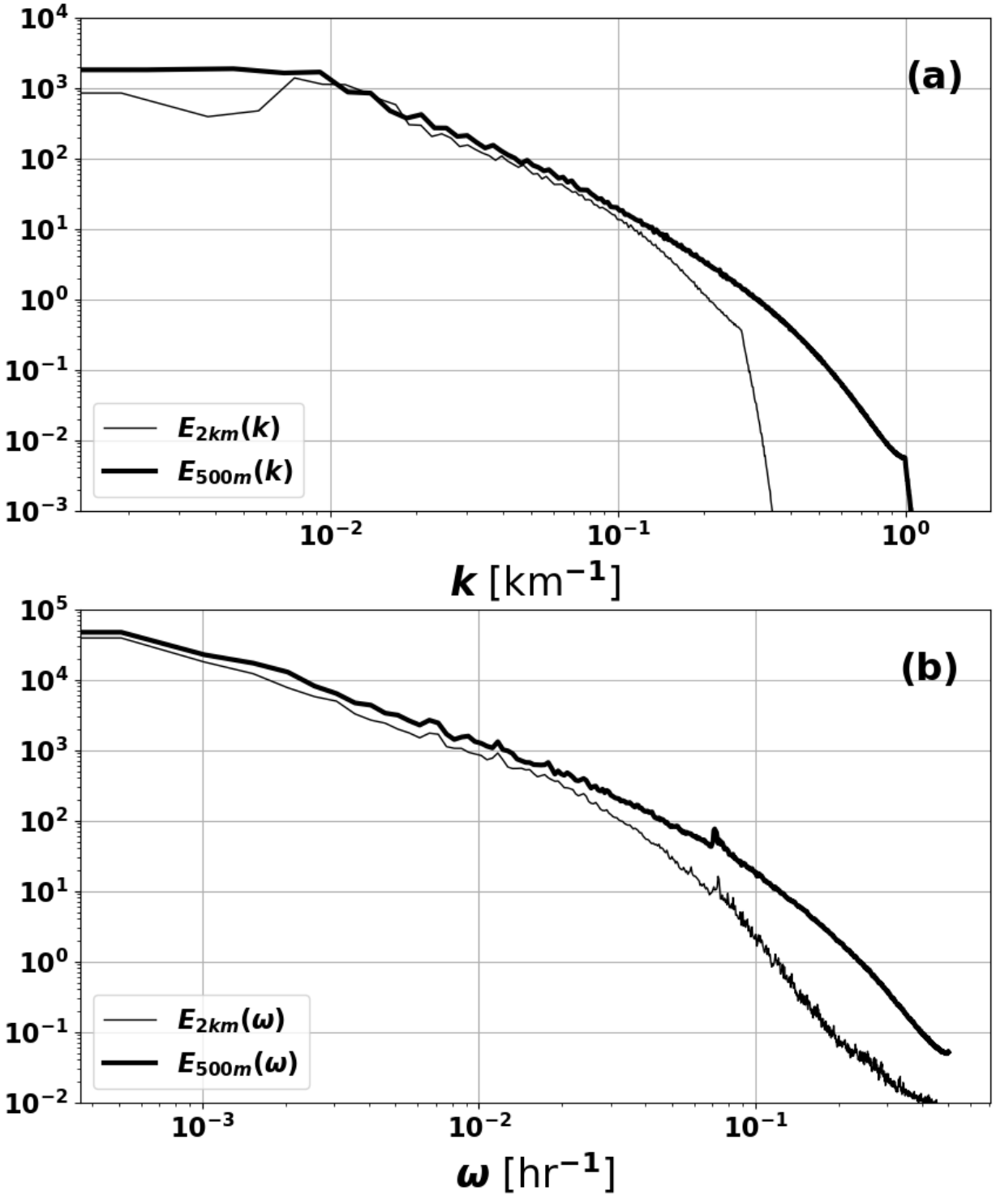

FIG. 7. (a) Spatial [m^2s^{-2}/(cycles/m)] and (b) temporal [m^2s^{-2}/(cycles/s)] kinetic energy spectrum averaged over the winter months of January, February and March for the 2 km run (thin line) and the 500 m run (thick line).

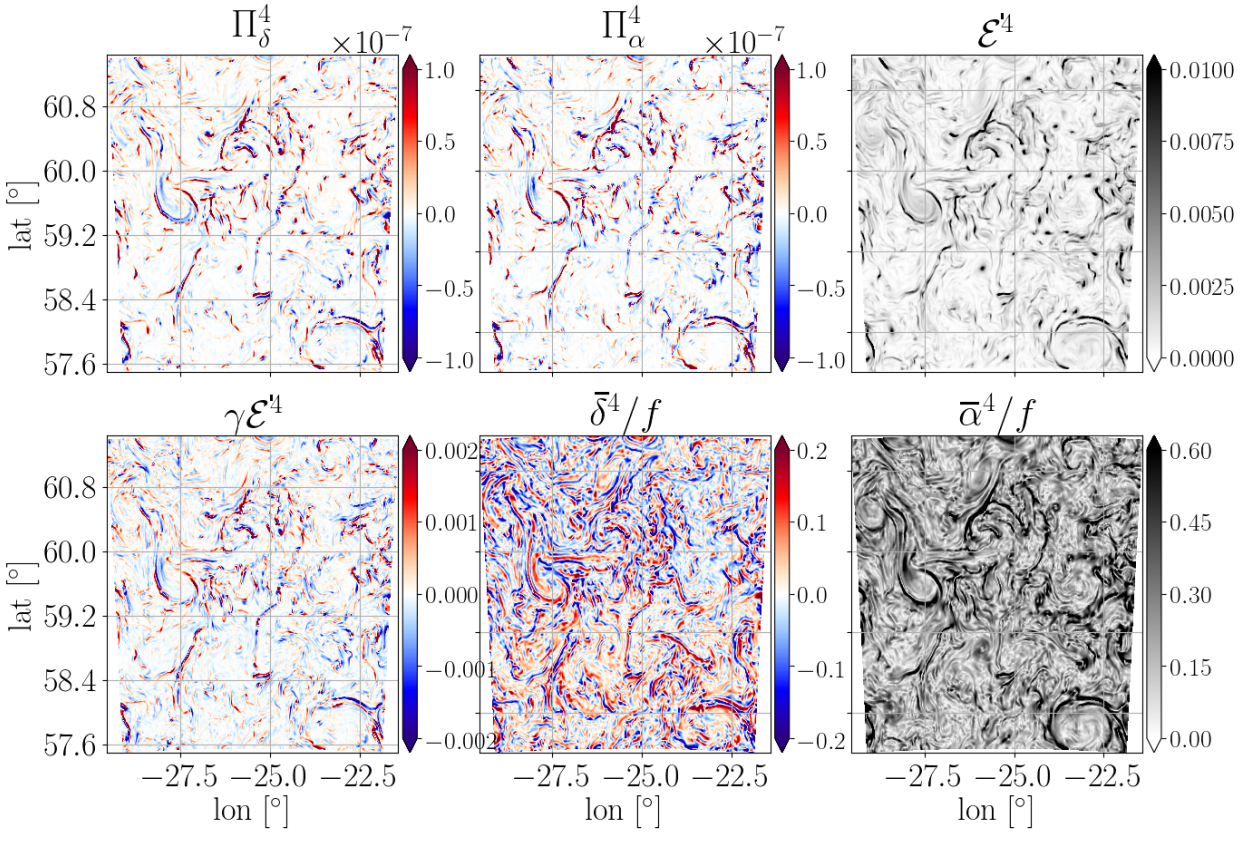

FIG. 8. The same snapshot as Fig. 1 showing the various components of Equation (8): the convergence production, Π^4_δ[m^{2}s^{-3}], the deformation shear production Π^4_α, where the superscript indicates $\ell = 4$ km ($\lambda_{sp} = 9.6$ km), i.e. Π^4 is the energy transferred from scales larger than 4 km to finer scales at a ocean surface. Also shown are the energy of the smaller scales $\mathcal{E}'^4$ [m^{2}s^{-2}], the anisotropy of the final scales in the local principal strain coordinates $\gamma\mathcal{E}'^4$, the larger scale divergence, $\bar{\delta}$ and the larger scale strain, $\bar{\alpha}$ normalized by the Coriolis paramter, f.

Π_δ breaks down at larger filter scales as is evident from Fig. 9 where a 12 km filter scale is used ($\lambda_{sp} = 28.8$ km). Π_δ is expectedly large where $\bar{\delta}$ is large and negative, however, Π_α is no longer correlated with the same in spite of structural similarities between the two fields; at larger scales (i.e. at scales of MLEs), even these similarities in spatial patterns break down.

c. Rotational and divergent components of the cross-scale energy flux

Given that the Π_α and Π_δ terms do not cleanly seperate mechanisms of inverse and forward energy fluxes, we decompose the horizontal velocity field into its rotational and divergent components,

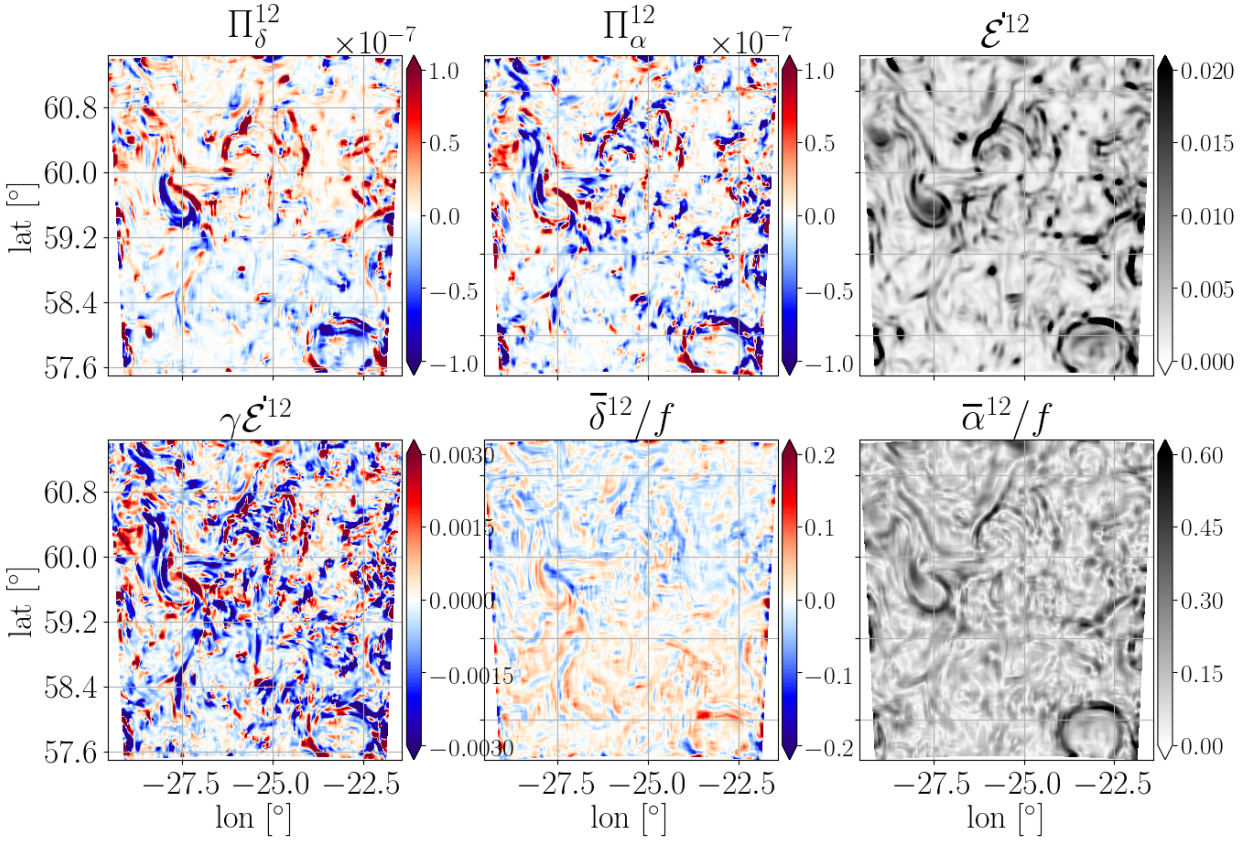

FIG. 9. Same as Fig. 8 but with a filter scale of $\ell = 12$ km ($\lambda_{sp} = 28.8$ km).

i.e. a Helmholtz decomposition, and subsequently compute energy transfers. Thus, we write

$$u = \phi_x + \psi_y\,, \tag{17}$$

$$v = \phi_y - \psi_x\,, \tag{18}$$

where ϕ and ψ are the velocity potential and streamfunction respectively. ϕ and ψ are solved by inverting the Poisson equations $\nabla^2\phi = \delta$ and $\nabla^2\psi = -\zeta$ assuming the simple Dirchlet boundary condition $\phi = 0$ at the boundary. We associate $(u_r, v_r) \equiv (\psi_y, -\psi_x)$ as the rotational component of the velocity and $(u_d, v_d) \equiv (\phi_y, \phi_x)$ as the divergent component. Note that once the Poisson equation for ϕ is inverted to obtain (u_d, v_d), (u_r, v_r) are obtained by simply subtracting the divergent components from the full velocity field so that the Poisson equation for ψ does not actually need to be solved. To keep the analysis simple, we first compute the energy fluxes through (10) using *only* the rotational components i.e. both the consituent fine-scale stresses and the coarse-scale strains that

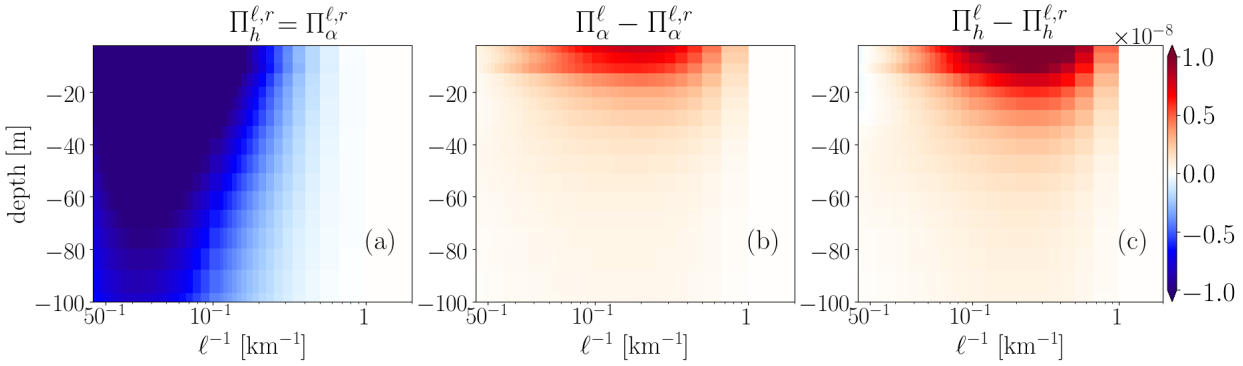

FIG. 10. (a) Spatiotemporally averaged energy flux $\Pi_\alpha^{\ell,r}$[m^{2}s^{-3}] (=$\Pi_h^{\ell,r}$) term computed purely using the rotational component of velocity. The corresponding $\Pi_\delta^{\ell,r}$ using only rotational components is trivially zero. (b) The difference between Π_α^{ℓ} and $\Pi_\alpha^{\ell,r}$ interpreted as the forward flux component of Π_α^{ℓ}. (c) The net forward energy flux component in Π_h^{ℓ} obtained by adding the result in (b) with that obtained in Fig. 5b; this is same as the difference between Π_h^{ℓ} and its purely rotational component, $\Pi_h^{\ell,r}$.

make up the energy flux are entirely rotational. We refer to the resulting horizontal energy transfer as $\Pi_h^{\ell,r}$, where the superscript refers to "completely rotational", noting that $\Pi_h^{\ell,r} = \Pi_\alpha^{\ell,r} + \Pi_\delta^{\ell,r}$. However, because $\Pi_\delta^{\ell} \propto \bar{\delta}$, we have that $\Pi_\delta^{\ell,r} \equiv 0$ and thus

$$\Pi_h^{\ell,r} = \Pi_\alpha^{\ell,r} \tag{19}$$

We plot the spatiotemporally averaged rotational component $\Pi_\alpha^{\ell,r}$ in Fig.10a and find it to be entirely upscale. The residual $\Pi_\alpha^{\ell} - \Pi_\alpha^{\ell,r}$ (Fig.10b) which includes a mix of rotational and divergent components, is almost entirely forward, implying that the purely rotation component, $\Pi_\alpha^{\ell,r}$ (equivalently $\Pi_h^{\ell,r}$ from (19)) accounts for the entirety of the inverse cascade of Π_h^{ℓ}. We associate this with the energetic interactions between MLEs through the mechanism demonstrated by Schubert et al. (2020) and also mesoscale eddies themselves. Adding this residual forward flux term to the other forward flux term found earlier, Π_δ^{ℓ} (Fig. 5c) gives us the total forward flux associated with the flow and this works out to be

$$\Pi_\delta^{\ell} + \Pi_\alpha^{\ell} - \Pi_\alpha^{\ell,r} = \Pi_h^{\ell} - \Pi_h^{\ell,r} \tag{20}$$

where we used the fact that $\Pi_{\delta}^{\ell,r}$ is identically zero. The total forward flux is plotted in Fig. 10c. In summary, using the helmholtz decomposition, we can decompose the total horizontal transfer Π_h^ℓ into the inverse energy flux, given by $\Pi_h^{\ell,r}$ comprising interactions among purely rotational components and the forward energy flux $\Pi_h^\ell - \Pi_h^{\ell,r}$ which includes a mix of the rotational and divergent components. This decomposition is dynamically relevant unlike an attempted forward-inverse decomposition by Schubert et al. (2020) who separately average the negative values and positive values of Π_h^ℓ to separate the forward and inverse fluxes. It is notable that the peak values of the forward (Fig. 10c) and inverse (Fig. 10a) fluxes are in fact comparable though the latter spans a larger range of spatial scales and has a deeper vertical extent. The reason of course is that forward energy flux is highly localized at fronts. But a casual examination of the spatiotemporal energy spectra (Fig. 11a-b) of the divergent and rotational fields can give the impression that the divergent component is dynamically insignificant compared to the rotational (note the order of magnitude smaller spectral density at submesocales), in contrast with the picture that emerges from Fig. 10c. Though of secondary importance to the present study, a key question is how both the magnitude of the forward flux and the ratio of the rotational and divergent spectra change with increasing horizontal resolutions. We address this in detail in an upcoming study.

At this point it must be clear that the results in this section could have been obtained directly from (4) or (10) without employing the principle strain coordinates or the $\alpha - \delta$ decomposition; all that was required was the Helmholtz decomposition. However, the real strength of this decomposition lies in the theoretical connections that are readily established with the asymptotic framework for frontogenesis discovered by Barkan et al. (2019) as discussed in Section 5.

5. The connection between energy flux at fronts and frontogenesis

Barkan et al. (2019) provided a broad theoretical framework for frontogenesis based on general scaling considerations for frontal Rossby number, $Ro = V/fl$ and the frontal anisotropy, $\epsilon = l/L$, where V is the along front velocity scale and l the frontal width, and L the along front length scale. Under the assumptions of

$$Ro \sim O(1), \qquad \epsilon \ll 1, \tag{21}$$

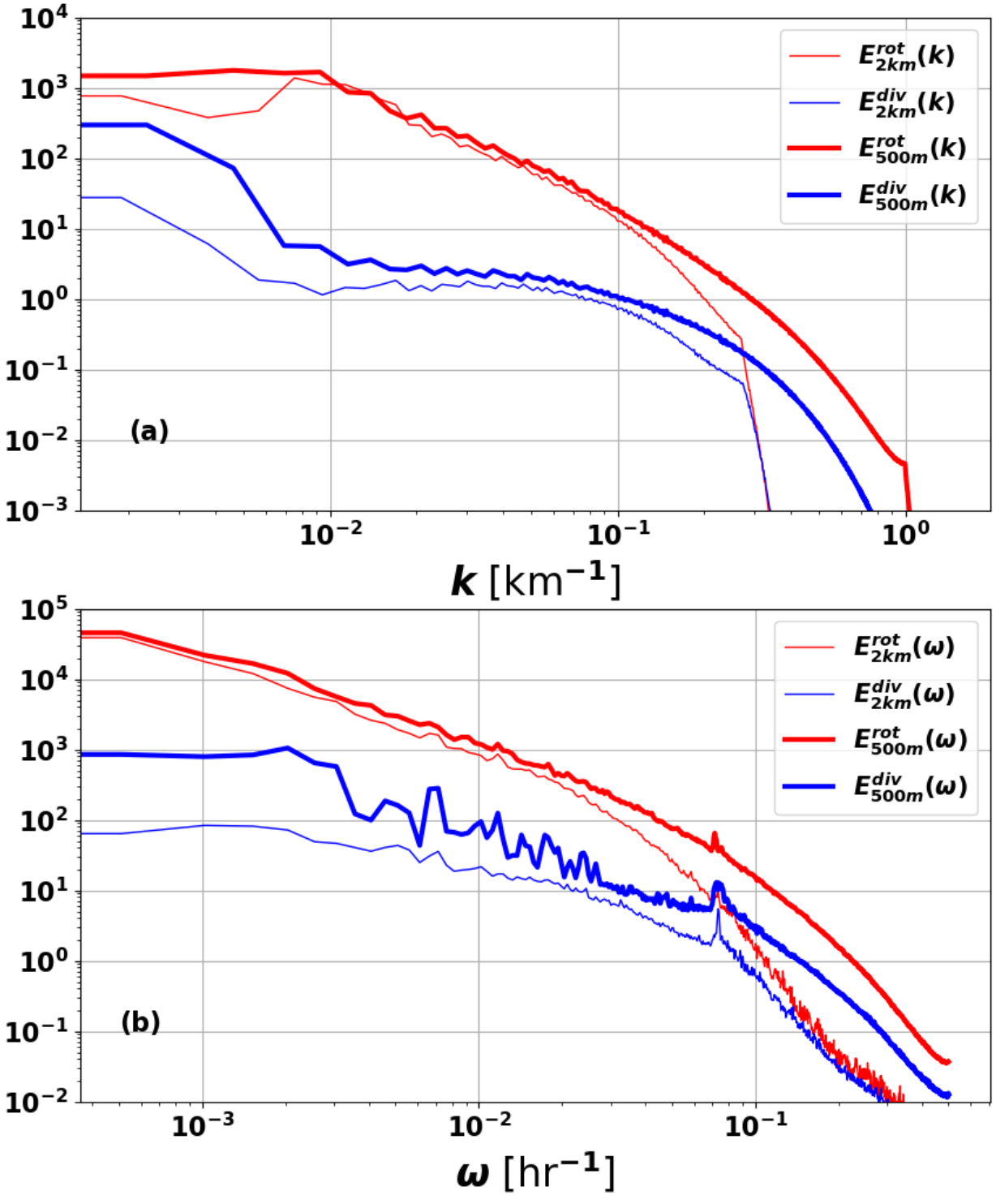

393 FIG. 11. (a) Spatial [m^2s^{-2}/(cycles/m)] and (b) temporal kinetic energy spectrum [m^2s^{-2}/(cycles/s)] of the
394 rotational (red lines) and divergent (blue lines) components of the flow averaged over the winter months of
395 January, February and March for the 2 km (thin lines) and 500 m (thick lines) run.

both of which are defining frontal characteristics, Barkan et al. (2019) were able to show after neglecting dissipative terms, that for fronts [2],

$$\frac{D\delta}{Dt} \sim -\delta^2, \tag{22}$$

$$\frac{D\zeta}{Dt} \sim -\zeta\delta \tag{23}$$

$$\frac{D|\nabla b|^2}{Dt} \sim -2|\nabla b|^2\delta\,. \tag{24}$$

Eq. (22) can be solved directly in a Lagrangian reference frame and was shown by Barkan et al. (2019) to have a finite-time singularity similar to the result by Hoskins and Bretherton (1972) derived under the less general semi-geostrophic approximation. Of course, the actual singularity cannot manifest and the rapid increase in the convergence $-\delta$ is arrested in practice by frontal instabilities (like symmetric or shear instabilities), or numerical dissipation in ocean models. From (23) and (24), both ζ and ∇b also have finite-time singularities.

The equations for the fine-scale kinetic energy, from (8), can be written in the form (Aluie et al. 2018),

$$\frac{D\mathcal{E}'}{Dt} + \nabla\cdot\mathcal{T} = -\bar{\delta}\mathcal{E}' + \gamma\mathcal{E}'\bar{\alpha} \tag{25}$$

where $\mathcal{T}$ is the fine-scale kinetic energy transport flux (for detailed forms, see Aluie et al. (2018) or the Appendix B in Barkan et al. (2017)). The similarities in the dominant terms describing the evolution of $|\nabla b|^2$ and $\mathcal{E}'$ as seen in (10) and (16) suggest that (25) can be written in a form similar to (24) under the frontal scalings (21). Here we neglect the vertical shear terms in both cases, which is justified in the scaling analysis of Barkan et al. (2019), supported by our model analysis; in particular Π_z [defined in (3)] is on average about 5 times smaller than Π_h (see Fig. 14). As a reminder, we note that while (25) involves coarse-grained quantities $\bar{\delta}$ and $\bar{\alpha}$, the frontogenetic equations (22)-(24) involve the actual fields themselves. Therefore these quantities are comparable in the limit when the filter-scale is smaller than the average frontal scale (in our case, $\ell \leq 10$ km or equivalently, $\lambda_{sp} \leq 24$ km).

While the principal strain coordinates lead to very compact forms for the energy transfer, the Π_α term can be difficult to interpret, principally owing to the opaqueness of the anisptropy term

[2]Two additional terms appear at leading order in the vorticity and divergence equations. These terms turn out to be subdominant as they cancel out with the vertical mixing terms through the turbulent thermal wind (TTW) balance that are not formally included in inviscid theory.

γ. Instead, for the remainder of this section we work in a front aligned coordinate system, with the y-axis being along the frontal axis and x being the cross-frontal axis. The along and crossfront velocities are v and u respectively. Working in this coordinate system, we employ the coordinate-free forms of energy transfer (10) and frontogenetic tendency (16). The frontal scaling assumptions (21) need to be supplemented by one for the velocities,

$$u \sim Ro\, v\,. \tag{26}$$

which crucially differs from the semigeostrophic approximation of Hoskins and Bretherton (1972) who always have $u \ll v$. But because oceanic fronts have $Ro = O(1)$, $u \sim v$ i.e. the alongfront and crossfront velocities have similar order. This is a crucial observation about oceanic fronts that separates the analysis in Hoskins and Bretherton (1972) and Barkan et al. (2019). For frontal coarse graining scales, we also assume that the coarse and fine velocities scale similarly. i.e.

$$\bar{u} \sim \bar{v}\,, \qquad u' \sim v'. \tag{27}$$

Thus we can infer that

$$\tau_{uu} \sim \tau_{vv} \sim \tau_{uv} \sim (\tau_{uu} + \tau_{vv})/2 = \mathcal{E}'\,. \tag{28}$$

Furthermore the crossfront gradients and alongfront gradients are related as

$$\partial_y \sim \epsilon \partial_x \Rightarrow \partial_y \ll \partial_x\,, \tag{29}$$

reflecting the crossfront gradients at fronts are a lot larger than alongfont gradients. From (29), we can infer that

$$\begin{aligned} \bar{\delta} &= \bar{u}_x + \bar{v}_y \\ &\sim \bar{u}_x \sim \bar{v}_x \\ &\sim \bar{v}_x - \bar{u}_y = \bar{\zeta}\,, \end{aligned} \tag{30}$$

i.e. $\bar{\delta} \sim \bar{\zeta}$ and that $\bar{\alpha}^2 \sim \bar{\delta}^2 + \bar{\zeta}^2$. Thus the strain comprises both divergent and rotational components. We can use the above scaling estimates to assess the energy transfer term Π_α using the coordinate

free form (10). First to estimate Π_α,

$$\begin{aligned}\Pi_\alpha =&(\tau_{uu}-\tau_{vv})(\bar{u}_x-\bar{v}_y)/2-\tau_{uv}(\bar{u}_y+\bar{v}_x)\\ &\sim -\tau_{uv}\bar{v}_x/2\sim -\mathcal{E}'\bar{u}_x\\ &\sim -\mathcal{E}'\bar{\delta}=\Pi_\delta\,,\end{aligned}\tag{31}$$

where we neglect the first term (because $\tau_{uu}\sim\tau_{vv}$) and the y-derivative in the second term (from (29)). Thus $\Pi_\alpha\sim\Pi_\delta$, supporting the model-based observation that Π_h has an equipartition at small scales. The scaling arguments used to infer this result fall short of an actual explanation for the striking similarity of the Π_α and Π_δ observed in Fig. 8 but provide a strong heuristic for the same. Then (25) can be written as

$$\frac{D\mathcal{E}'}{Dt}+\nabla\cdot\mathcal{T}\sim -2\bar{\delta}\mathcal{E}'\,,\tag{32}$$

where we use $\Pi_\alpha\sim\Pi_\delta=-\mathcal{E}'\bar{\delta}$. Thus the evolution equation (32) takes the same form as (24). Because the equipartition demonstrated here is asymptotic, the precise numerical factor of 2 multiplying $-\bar{\delta}\mathcal{E}'$ is not expected in general. In the simple model-based computation in Fig. 2, for example, the numerical factor is actually around 2.5 although that calulation depended on some specific choices for the frontal averaging which could affect the factor obtained. We also note the connection between the result obtained here, namely $-2\bar{\delta}\mathcal{E}'$ as the forward cascade at fronts, and that from the Helmholtz decomposition, $\Pi_h^\ell-\Pi_h^{\ell,r}$; the latter expression consists of a mix of rotational and divergent components which is consistent with the fact that although $\bar{\delta}$ is purely divergent, $\mathcal{E}'$ comprises both rotational and divergent velocity fields.

For completeness, we derive (24) starting from the coordinate-free form in (16). From (29), using $b_y^2\ll b_x^2$ and $b_xb_y\ll b_x^2$, we get

$$\begin{aligned}\mathcal{B}_\alpha &= (b_x^2-b_y^2)(u_x-v_y)/2-b_xb_y(u_y+v_x)\\ &\sim -b_x^2u_x/2\\ &\sim -(b_x^2+b_y^2)\frac{\delta}{2}=\mathcal{B}_\delta\,,\end{aligned}\tag{33}$$

which leads to (24). Interestingly, as in the case of (31), (33) also demonstrates an equipartition in the α and δ terms but the dominant terms are different. Now, because we associate the evolution

of ∇b through (24), it also follows that we associate the forward energy cascade at fronts as being primarily caused due to frontogenesis. This is, in retrospect, expected because the rapid increase in the convergence through (22) can be interpreted as a correspondingly rapid shrinkage in the frontal scale, l associated with the frontal velocities, u and v. In other words, frontogenesis is the primary cause of forward energy cascade at fronts.

The mechanism elucidated above can be connected to the broader energetics of the surface mixed layer as follows: Mixed layer instabilities which are strongest during the winter convert mixed layer available potential energy to kinetic energy of fronts and MLEs. Frontogenesis transfers energy at fronts to smaller scales by the mechanism proposed by Barkan et al. (2019) as demonstrated here, while mixed layer eddies undergo an inverse cascade of energy to mesoscales as shown by Schubert et al. (2020). Of course, this framing presumes that no competing mechanisms are present, chief among them being symmetric instability which is likely not resolved at the 500 m model resolution employed here. We discuss this last point further in Section 6b.

6. Discussion

a. The dependence of energy transfer on effective flow resolution

The 2 km solution, as seen in Figures 5 and 4 fails to not only resolve the forward cascade but underestimates the submesoscale inverse cascade signal too. The reason for this is that the 2 km model has a larger amount of numerical dissipation, which in ROMS is a grid dependent implicit biharmonic dissipation i.e. lower resolutions are more dissipative and therefore can suppress advective dynamics that lie closer to the grid resolution. Other studies have noted this increase in upscale energy flux as the resolution is increased towards submesoscale-permitting resolutions Kjellsson and Zanna (2017); Qiu et al. (2014). When computing energy transfers from observations, however, the key issue is one of spatiotemporal resolution of the measured data (unlike models where the issue is innacurate physics). To study how spatial sampling affects the energy transfer without the added effects of spurious physics (through higher numerical dissipation), we treat the 500 m run as the *ground truth* solution and smooth the flow fields with systematically larger filter sizes and compute the crosscale energy fluxes of the smoothed fields. The actual fidelity of the 500 m run is not of particular importance; while it plausibly resolves the MLE inverse energy cascade accurately, it is likely that higher resolution runs would modify the forward energy flux.

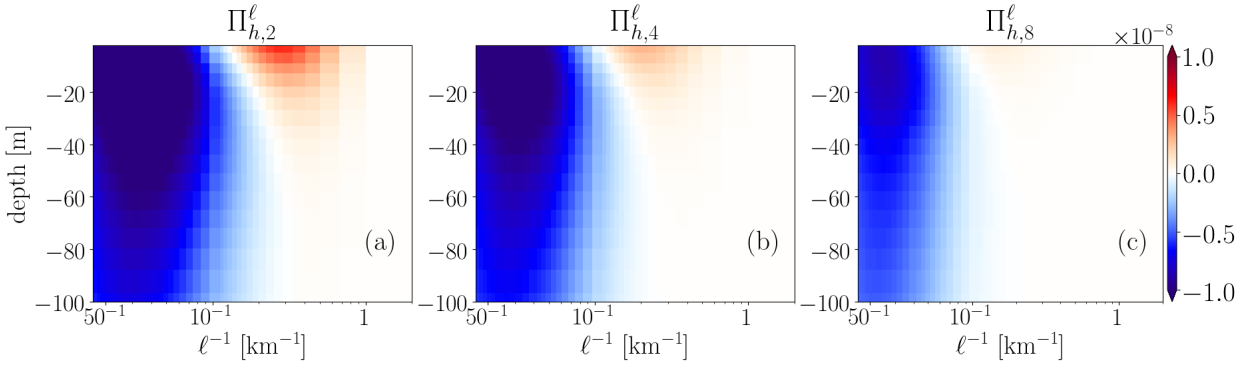

494 FIG. 12. Spatiotemporally averaged horizontal energy flux [m^2s^{-3}] for the 500 m resolution run, with uniform
495 smoothing performed on the velocity fields before computing the fluxes. The subscripts denote the smoothing
496 filterwidth with values (a) 2 km (b) 4km and (c) 8km. These results are directly comparable to the unsmoothed
497 energy transfer in Fig. 5a.

517 Figure 12 shows the spatiotemporally averaged fluxes for increasing values of smoothing scale (a
518 simple uniform filter is applied in each case). Comparing Fig. 12a, which has a 2 km smoothing,
519 with the corresponding results from the 2 km model (Fig. 5d) and the 500 m model (Fig. 5a), we
520 find that about half of the forward cascade and most of the inverse cascade region is accurately
521 captured. The 4km smoothed fields have fluxes that resemble the 2 km model fluxes without a trace
522 of the forward flux captured while the upscale flux is also diminished. The 8km smoothed fields
523 (Fig. 12c) have almost no forward fluxes and substantially weaker upscale fluxes, suggesting that
524 observations would need an average spatial resolution of at least 8km at this latitude to capture any
525 fraction of the submesocale energy fluxes. In Fig. 13 we also plot the spatial spectra corresponding
526 to these smoothed fields. An interesting observation is the effect of the uniform filter on the spatial
527 spectrum of the flow. For example, the 2km filter smoothed field has a rapid spectral drop off
528 between 4 km and 5 km allowing us to infer that spectral cutoff is between 2 and 2.5 times the filter
529 scale. However, it can be difficult to discern a single length scale as the effective spectral cutoff of
530 the uniform filter given the continous drop off starting from around 5 km scales of the 2km-filtered
531 field (the red curve in Fig. 13). Unlike the spectrum however, the energy flux is a direct diagnostic
532 of the dynamics allowing us to infer the effective spectral cutoff of the uniform filter, as has been
533 done in Fig. 6 (Sec. 4a) where a factor of 2.4 was found.

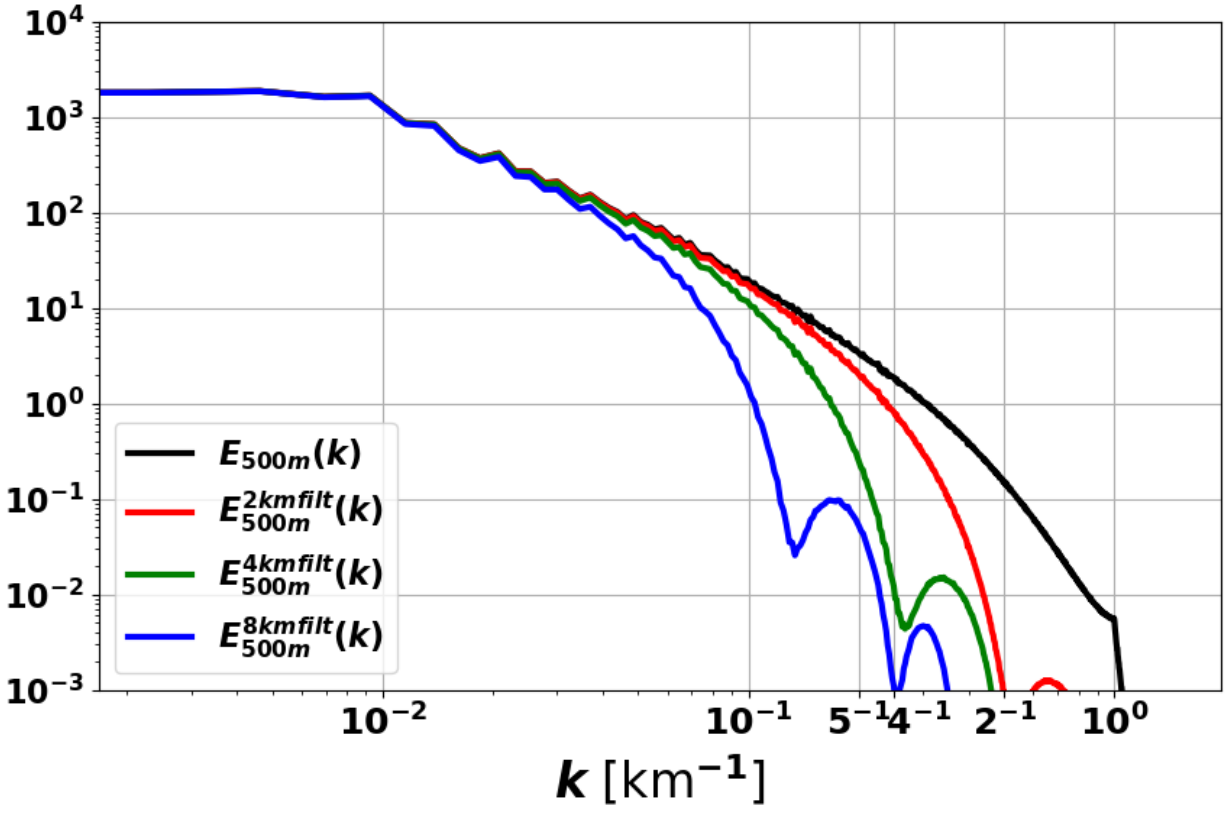

FIG. 13. (a) Spatial energy spectra [m^2s^{-2}/(cycles/m)] of the velocity fields used to compute the energy flux for smoothing performed by different uniform filter sizes in Fig. 12. The red, green and blue curves correspond to Fig. 12a, b and c respectively. The black curve is the spectrum of the unsmoothed velocity field, replotted from Fig. 7a for reference. Note that the 2km-smoothed field (red) starts dropping off between 4 km and 5km scales.

b. Symmetric instability: A competing and downstream mechanism for forward energy flux

Symmetric Instability (SI) is a form of negative potential vorticity (PV) instability (Hoskins 1974; Jones and Thorpe 1992; Thomas et al. 2013; Bachman and Taylor 2014; Yu et al. 2019) which occurs in the surface mixed layer when the potential vorticity of fronts is decreased through the action of surface wind stresses or diabatic cooling. Because frontal PV can be written as (assuming geostrophic fronts)

$$q = f(\zeta + f)b_z - |\nabla b|^2 \tag{34}$$

fronts with stronger buoyancy gradients are more likely to undergo SI. In the event that strong fronts do develop negative PV due to the action of surface forcing the front undergoes SI (referred specifically as *forced* SI), transferring energy to three-dimensional fine scale motions (i.e. a forward energy flux) through the vertical flux term Π_v^ℓ (more specifically the vertical flux term with the geostrophic coarse scale vertical shear, or the geostrophic shear production, GSP) in the process bringing the frontal PV to zero and restratifying the mixed layer.

Unlike the frontal forward mechanism demonstrated in this manuscript, SI is not a generic mechanism and depends crucially on the strength of fronts and the local surface forcing therein. For example a surface wind stress can generate negative PV fluxes through the so-called Ekman buoyancy fluxes but are strongly contingent on the direction of the wind stress relative to the front alignment; downfront winds being most favorable for inducing forced SI (Thomas and Lee 2005). Furthermore, the boundary layer turbulence mediated ageostrophic secondary circulation, also referred to as a turbulent thermal wind (TTW) balance (McWilliams et al. 2015; Wenegrat and McPhaden 2016; McWilliams 2017; Crowe and Taylor 2018), acts as a source of PV in the surface mixed layer which could potentially offset SI at oceanic fronts (Wenegrat et al. 2018). Given that the TTW mechanism is pervasive in submesoscale-resolving ocean models (McWilliams et al. 2015; Wenegrat et al. 2018; Barkan et al. 2019), this could be a relevant offsetting mechanism for SI. In our present model runs, the vertical flux, Π_v^ℓ is on average 4 times smaller than Π_h^ℓ as is evident in Fig. 14a. Π_v^ℓ also has a rather different structure than Π_h^ℓ (Fig. 5a) with a forward flux close to the surface and a near-surface upscale flux. The spatiotemporally averaged geostrophic shear production,

$$\Pi_{vg}^\ell = -(\overline{u'w'}u_{z,g} + \overline{u'w'}v_{z,g}), \tag{35}$$

where the geostrophic shear is $(u_{z,g}, v_{z,g}) \equiv (-by,\ bx)/f$, is plotted as a function of ℓ in Fig. 14b. Π_{vg}^ℓ is largest at frontal scales but is *upscale* instead of downscale as might be expected if SI was a dominant process on average at these scales in our 500 m model run during winter. Note that this does not preclude the local importance of SI at strong density fronts with favorable wind stress. The structure of Π_v^ℓ (Fig. 14a) is likely a consequence of interactions between mesoscale and submesoscale eddies and IGWs (Barkan et al. 2021) and are not like the cascade processes that determine the structure of Π_h^ℓ. While IGWs in the present class of runs are rather weak, some level are likely present through the interaction of currents with bottom topography and the projection of

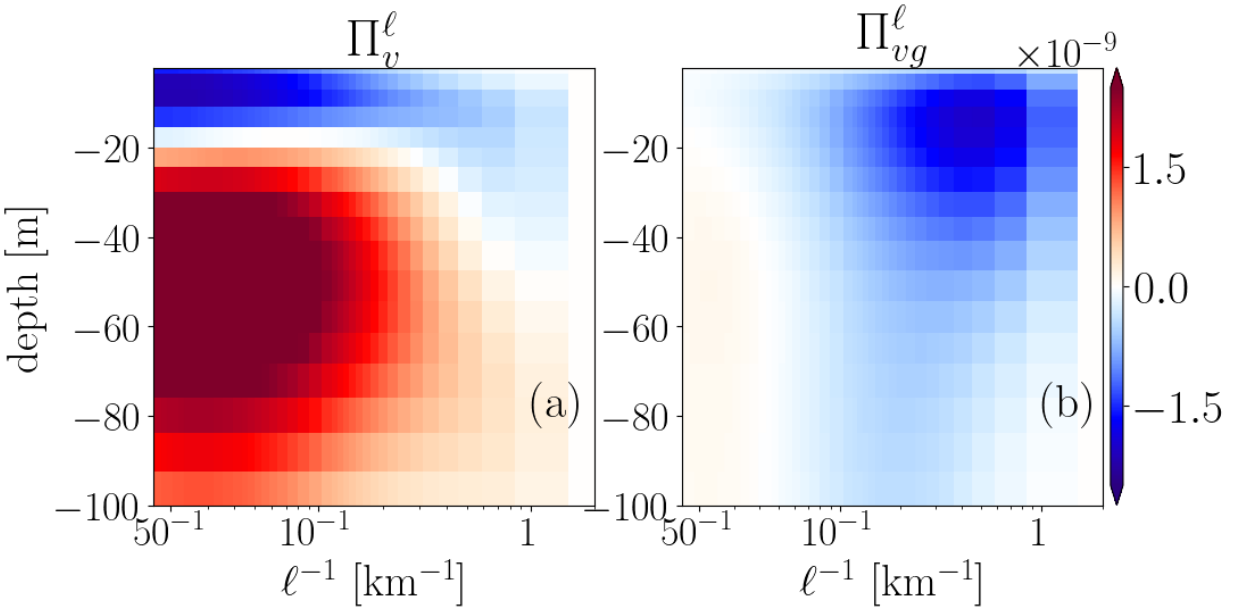

FIG. 14. Spatiotemporally averaged a) vertical shear energy flux, Π_v^ℓ [m^{2}s^{-3}] and b) the geostrophic shear production, Π_{vg}^ℓ, (defined in (35)) for the 500 m resolution run during winter months. Note that the colorbar ranges are 4 times smaller than the corresponding horizontal flux figures in the rest of this study. i.e. Π_v^ℓ is on average 4 times smaller than Π_h^ℓ.

the daily forced wind stress onto inertial motions. In the presence of wind and tide-generate IGWs, however, Π_v^ℓ is of similar order to Π_h^ℓ (Barkan et al. 2021).

Recently Dong et al. (2021b) studied an idealized front forced by downfront wind that subsequently underwent SI. They found that in the absence of a SI-specific paramterization (Bachman et al. 2017) supplementing the surface boundary layer parameterization (in their case, as in ours, KPP) SI is suppressed and the GSP term is underestimated. We expect a similar lack of SI in our model results given the lack of an SI parameterization, an issue that we expect to remedy in future studies. Also, another recent paper (Dong et al. 2021a) used a global submesoscale permitting model solution to estimate the horizontal scale of SI in the ocean which would also correspond to the horizontal resolution at which SI could be potentially resolved in ocean models. They find that in general, the resolutions required are below 100 m in a majority of the ocean, consideraly higher than the 500 m model used here. Although, concurrent work by (Jing et al. 2021) did find evidence for SI along the fronts flanking the mesoscale eddies that formed part of the subtropical countercurrent (STCC) during the summer (when the STCC eddies are most energetic) in the

Northwest Pacific, in a 500 m horizontal resolution model run. Because the STCC is a zonal current, favorable downfront winds make the presence of SI in the summer in that region likely. Whether such favorable surface forcing conditions exist in this region and their role in triggering SI remains to be examined. Also of importance is the role of the mechanism of frontogenesis - in summer mesoscale strain-induced frontogeneris is more likely to be important (as in the case of STCC) whereas in winter mixed-layer instability in conjunction with TTW is more plausible; as explained above, TTW can offset SI.

7. Summary

In this study we examine the flux of kinetic energy across spatial and temporal scales in submesoscale resolving simulations of the North Atlantic Ocean, focusing on the Iceland basin region. Instead of the traditionally used spectral energy flux approach, we use the coarse-graining method to compute the fluxes (Aluie et al. 2018). The coarse-graining approach involves a decomposition of the flow into slow (large) and fast (small) components using a temporal (spatial) smoothing filter; the equations for the kinetic energy of the coarse (large or slow) and fine (small or fast) components are then written and the terms corresponding to the energy exchange (or equivalently the energy flux from coarse to the fine scales) between the two components are identified. Following recent work (Aluie et al. 2018; Schubert et al. 2020; Barkan et al. 2021), we analyze the cross-scale energy flux in two ways. First, we average the flux over the horizontal domain and over the analysis time period (here the winter months of January to March) and examine the average flux as a function of filterscale and depth. Second, for specific filter scales and at a specific depth (here, near the surface) we visualize the spatial structure of the flux and examine its patterns relative to observed flow structures like mesoscale and mixed-layer eddies and submesoscale fronts. Our objective here is to identify the nature of the cross-scale energy flux at O(1-10) km length scales, that typically correspond to submesoscale currents in the ocean, comprising mixed-layer eddies (MLEs) and fronts that are generally limited to the near-surface mixed layer and particularly strong in the winter months due to the presence of deep mixed layers.

A plethora of studies over the past two decades, starting from Capet et al. (2008) have found that submesoscales have a dual cascade of energy, an inverse cascade to mesocale eddies and a forward energy cascade to dissipation scales. Recent work by Schubert et al. (2020) also employing the

coarse-graining approach used here, were able to show that MLEs undergo an inverse cascade of energy to mesoscales, in particular providing a visual demonstration of the 'absorption' of MLEs into mesoscale eddies. They also highlighted a forward energy flux at fronts without providing a physical explanation for this phenomenon. In this study we provide the mechanism for the frontal forward cascade through model-based analysis and by extending a recently proposed asymptotic theory for frontogenesis (Barkan et al. 2019).

In order to shed light on the mechanism of the frontal forward flux we pursue two concurrent approaches building on the coarse-graining framework. First we decompose the flow field into rotational and divergent components i.e. a Helmholtz decomposition. We then compute the cross-scale flux purely due to the rotational velocity components. This rotational flux is found, on spatio-temporal averaging, to be almost entirely upscale (i.e. an inverse cascade) in the upper ocean. The difference between the total flux and the rotational flux is found to be, on average, entirely downscale (i.e. a forward cascade). In other words the Helmholtz decomposition neatly decomposes the inverse and forward energy flux components of the flow.

Concurrently, we write the cross-scale energy flux in the principal strain coordinates, where the coarse (or smoothed by the filter) field strain tensor is diagonalized. This allows the flux to be written in a simple sum of two components where the first component is proportional to the coarse strain, $\bar{\alpha}$ and the second component is proportional to the convergence (i.e. negative divergence) of the coarse field, $-\bar{\delta}$, where $\bar{(\cdot)}$ denotes the filter-based smoothing operator. Calculating these two components in the model data, we find that the $\bar{\alpha}$ component consists (on average) of most of the inverse energy flux but the total forward flux is equipartioned between the $\bar{\alpha}$ and $\bar{\delta}$ components. We then use the asymptotic theory of frontogenesis proposed by Barkan et al. (2019) to theoretically demonstrate the equipartition of the forward energy flux at fronts between the $\bar{\alpha}$ and $\bar{\delta}$ terms (Section 5) for fronts. But this equipartion also means that, because the $\bar{\delta}$ component of flux is proportional to the convergence, $-\bar{\delta}$, so is the $\bar{\alpha}$ component and consequently so is the total energy flux at fronts (which is just a sum of the two components). Note that because fronts are convergent flows ($\delta < 0$), this essentially provides a theoretical and numerical basis for the forward energy flux at fronts. Furthermore, in the asymptotic theory of frontogenesis by Barkan et al. (2019), a crucial result was that the Lagrangian rate of change (i.e. D/Dt) of frontal quantities like vorticity, divergence and buoyancy gradient were all proportional to $-\delta$ which at fronts is

positive. This causes a finite time singularity in the convergence and correspondingly in the other frontal quantities i.e. frontogenesis. The fact that the rate of change of the fine scale kinetic energy, i.e. the cross-scale energy flux is also proportional to $-\bar{\delta}$ allows us to infer that the cause of the forward energy flux at fronts is actually frontogenesis (noting that δ and $\bar{\delta}$ are similar when the coarse-graining scale is around frontal scales). Heuristically this is because the sharpening of fronts due to frontogenesis essentially transfers the frontal energy to smaller scales resulting in a forward energy flux.

Acknowledgments. Kaushik Srinivasan, Roy Barkan and James C. McWilliams were supported by ONR-N000141812697. Roy Barkan was further supported by NSF Grant OCE-1851397 and Israeli Science foundation Grant 1736/18. James C. McWilliams was further supported ONR-N000141812599 and ONR N000142012023. Computation of model simulations and most of the scale-to-scale analysis used here was perfomed on Extreme Science and Engineering Discovery Environment (XSEDE) clusters (Towns et al. 2014).

References

Ajayi, A., J. Le Sommer, E. P. Chassignet, J.-M. Molines, X. Xu, A. Albert, and W. Dewar, 2021: Diagnosing cross-scale kinetic energy exchanges from two submesoscale permitting ocean models. *Journal of Advances in Modeling Earth Systems*, e2019MS001923.

Alford, M. H., J. A. MacKinnon, H. L. Simmons, and J. D. Nash, 2016: Near-inertial internal gravity waves in the ocean. *Annual review of marine science*, **8**, 95–123.

Aluie, H., M. Hecht, and G. K. Vallis, 2018: Mapping the energy cascade in the North Atlantic Ocean: The coarse-graining approach. *J. Phys. Oceanogr.*, **48 (2)**, 225–244.

Bachman, S. D., B. Fox-Kemper, J. R. Taylor, and L. N. Thomas, 2017: Parameterization of frontal symmetric instabilities. i: Theory for resolved fronts. *Ocean Modelling*, **109**, 72–95.

Bachman, S. D., and J. R. Taylor, 2014: Modelling of partially-resolved oceanic symmetric instability. *Ocean Modelling*, **82**, 15–27.

Balwada, D., Q. Xiao, S. Smith, R. Abernathey, and A. R. Gray, 2021: Vertical fluxes conditioned on vorticity and strain reveal submesoscale ventilation. *Journal of Physical Oceanography*.

673 Barkan, R., M. J. Molemaker, K. Srinivasan, J. C. McWilliams, and E. A. D'Asaro, 2019: The role
674 of horizontal divergence in submesoscale frontogenesis. *Journal of Physical Oceanography*,
675 **49 (6)**, 1593–1618.

676 Barkan, R., K. Srinivasan, L. Yang, , J. C. McWilliams, J. Gula, and C. Vic, 2021: Oceanic cross-
677 scale energy transfers under the influence of internal waves. *Geophysical Research Letters*, **0 (0)**,
678 10–20.

679 Barkan, R., K. B. Winters, and J. C. McWilliams, 2017: Stimulated imbalance and the enhancement
680 of eddy kinetic energy dissipation by internal waves. *J. Phys. Oceanogr.*, **47 (1)**, 181–198.

681 Barkan, R., K. B. Winters, and S. G. L. Smith, 2015: Energy cascades and loss of balance in a
682 reentrant channel forced by wind stress and buoyancy fluxes. *Journal of Physical Oceanography*,
683 **45 (1)**, 272–293.

684 Boccaletti, G., R. Ferrari, and B. Fox-Kemper, 2007: Mixed layer instabilities and restratification.
685 *J. Phys. Oceanogr.*, **37 (9)**, 2228–2250.

686 Brannigan, L., D. P. Marshall, A. Naveira-Garabato, and A. G. Nurser, 2015: The seasonal cycle
687 of submesoscale flows. *Ocean Modell.*, **92**, 69–84.

688 Callies, J., R. Ferrari, J. M. Klymak, and J. Gula, 2015: Seasonality in submesoscale turbulence.
689 *Nat. Commun.*, **6**, 6862.

690 Callies, J., G. Flierl, R. Ferrari, and B. Fox-Kemper, 2016: The role of mixed-layer instabilities in
691 submesoscale turbulence. *Journal of Fluid Mechanics*, **788**, 5–41.

692 Capet, X., J. C. McWilliams, M. J. Molemaker, and A. F. Shchepetkin, 2008: Mesoscale to
693 submesoscale transition in the California Current System. Part III: Energy balance and flux. *J.*
694 *Phys. Oceanogr.*, **38**, 44–64, doi:10.1175/2008JPO3810.1.

695 Crowe, M. N., and J. R. Taylor, 2018: The evolution of a front in turbulent thermal wind balance.
696 part 1. theory. *Journal of Fluid Mechanics*, **850**, 179–211.

697 Dong, J., B. Fox-Kemper, H. Zhang, and C. Dong, 2021a: The scale and activity of symmetric
698 instability estimated from a global submesoscale-permitting ocean model. *Journal of Physical*
699 *Oceanography*, **51 (5)**, 1655–1670.

Dong, J., B. Fox-Kemper, J. Zhu, and C. Dong, 2021b: Application of symmetric instability parameterization in the coastal and regional ocean community model (croco). *Journal of Advances in Modeling Earth Systems*, **13 (3)**, e2020MS002 302.

Eyink, G. L., and H. Aluie, 2009: Localness of energy cascade in hydrodynamic turbulence. I. Smooth coarse graining. *Phys. of Fluids*, **21 (11)**, 115 107.

Ferrari, R., and C. Wunsch, 2009: Ocean circulation kinetic energy: Reservoirs, sources, and sinks. *Annual Review of Fluid Mechanics*, **41**.

Garabato, A. C. N., X. Yu, J. Callies, R. Barkan, K. L. Polzin, and E. E. Frajka-Williams, 2021: Kinetic energy transfers between mesoscale and submesoscale motions. *Journal of Physical Oceanography*.

Hoskins, B., 1974: The role of potential vorticity in symmetric stability and instability. *Quarterly Journal of the Royal Meteorological Society*, **100 (425)**, 480–482.

Hoskins, B. J., and F. P. Bretherton, 1972: Atmospheric frontogenesis models: Mathematical formulation and solution. *J. Atmos. Sci.*, **29 (1)**, 11–37.

Huang, H.-P., and W. A. Robinson, 1998: Two-dimensional turbulence and persistent zonal jets in a global barotropic model. *Journal of the atmospheric sciences*, **55 (4)**, 611–632.

Hypolite, D., L. Romero, J. C. McWilliams, and D. P. Dauhajre, 2021: Surface gravity wave effects on submesoscale currents in the open ocean. *Journal of Physical Oceanography*, **51 (11)**, 3365–3383.

Jing, Z., B. Fox-Kemper, H. Cao, R. Zheng, and Y. Du, 2021: Submesoscale fronts and their dynamical processes associated with symmetric instability in the northwest pacific subtropical ocean. *Journal of Physical Oceanography*, **51 (1)**, 83–100.

Jing, Z., L. Wu, and X. Ma, 2017: Energy exchange between the mesoscale oceanic eddies and wind-forced near-inertial oscillations. *Journal of Physical Oceanography*, **47 (3)**, 721–733.

Jones, S. C., and A. J. Thorpe, 1992: The three-dimensional nature of 'symmetric'instability. *Quarterly Journal of the Royal Meteorological Society*, **118 (504)**, 227–258.

Kjellsson, J., and L. Zanna, 2017: The impact of horizontal resolution on energy transfers in global ocean models. *Fluids*, **2 (3)**, 45.

Leonard, A., 1975: Energy cascade in large-eddy simulations of turbulent fluid flows. *Advances in geophysics*, Vol. 18, Elsevier, 237–248.

Ma, X., and Coauthors, 2016: Western boundary currents regulated by interaction between ocean eddies and the atmosphere. *Nature*, **535 (7613)**, 533–537.

McWilliams, J. C., 2016: Submesoscale currents in the ocean. *Proc. R. Soc. A*, The Royal Society, Vol. 472, 20160117.

McWilliams, J. C., 2017: Submesoscale surface fronts and filaments: Secondary circulation, buoyancy flux, and frontogenesis. *Journal of Fluid Mechanics*, **823**, 391.

McWilliams, J. C., J. Gula, M. J. Molemaker, L. Renault, and A. F. Shchepetkin, 2015: Filament frontogenesis by boundary layer turbulence. *J. Phys. Oceanogr.*, **45 (8)**, 1988–2005.

Mensa, J. A., Z. Garraffo, A. Griffa, T. M. Özgökmen, A. Haza, and M. Veneziani, 2013: Seasonality of the submesoscale dynamics in the Gulf Stream region. *Ocean Dynamics*, **63 (8)**, 923–941.

Molemaker, M. J., J. C. McWilliams, and X. Capet, 2010: Balanced and unbalanced routes to dissipation in an equilibrated Eady flow. *J. Fluid Mech.*, **654**, 33–63.

Polzin, K. L., 2010: Mesoscale eddy–internal wave coupling. part ii: Energetics and results from polymode. *Journal of physical oceanography*, **40 (4)**, 789–801.

Qiu, B., S. Chen, P. Klein, H. Sasaki, and Y. Sasai, 2014: Seasonal mesoscale and submesoscale eddy variability along the north pacific subtropical countercurrent. *Journal of Physical Oceanography*, **44 (12)**, 3079–3098.

Rai, S., M. Hecht, M. Maltrud, and H. Aluie, 2021: Scale of oceanic eddy killing by wind from global satellite observations. *Science Advances*, **7 (28)**, eabf4920.

Renault, L., P. Marchesiello, S. Masson, and J. C. Mcwilliams, 2019: Remarkable control of western boundary currents by eddy killing, a mechanical air-sea coupling process. *Geophysical Research Letters*, **46 (5)**, 2743–2751.

Renault, L., J. C. McWilliams, and J. Gula, 2018: Dampening of submesoscale currents by air-sea stress coupling in the californian upwelling system. *Scientific reports*, **8 (1)**, 1–8.

Renault, L., M. J. Molemaker, J. C. McWilliams, A. F. Shchepetkin, F. Lemarié, D. Chelton, S. Illig, and A. Hall, 2016: Modulation of wind work by oceanic current interaction with the atmosphere. *Journal of Physical Oceanography*, **46 (6)**, 1685–1704.

Rocha, C. B., G. L. Wagner, and W. R. Young, 2018: Stimulated generation: extraction of energy from balanced flow by near-inertial waves. *Journal of Fluid Mechanics*, **847**, 417–451.

Salmon, R., 1998: *Lectures on Geophysical Fluid Dynamics*. Oxford University Press.

Schubert, R., J. Gula, R. J. Greatbatch, B. Baschek, and A. Biastoch, 2020: The submesoscale kinetic energy cascade: Mesoscale absorption of submesoscale mixed layer eddies and frontal downscale fluxes. *Journal of Physical Oceanography*, **50 (9)**, 2573–2589.

Scott, R. B., and B. K. Arbic, 2007: Spectral energy fluxes in geostrophic turbulence: Implications for ocean energetics. *Journal of physical oceanography*, **37 (3)**, 673–688.

Scott, R. B., and F. Wang, 2005: Direct evidence of an oceanic inverse kinetic energy cascade from satellite altimetry. *Journal of Physical Oceanography*, **35 (9)**, 1650–1666.

Shchepetkin, A. F., and J. C. McWilliams, 2005: The Regional Oceanic Modeling System (ROMS): A split-explicit, free-surface, topography-following-coordinate oceanic model. *Ocean Modelling*, **9 (4)**, 347–404, doi:10.1016/j.OCEMOD.2004.08.002.

Srinivasan, K., J. C. McWilliams, and A. Jagannathan, 2021: High vertical shear and dissipation in equatorial topographic wakes. *Journal of Physical Oceanography*, **51 (6)**, 1985–2001.

Srinivasan, K., J. C. McWilliams, M. J. Molemaker, and R. Barkan, 2019: Submesoscale vortical wakes in the lee of topography. *Journal of Physical Oceanography*, **49 (7)**, 1949–1971.

Srinivasan, K., J. C. McWilliams, L. Renault, H. G. Hristova, J. Molemaker, and W. S. Kessler, 2017: Topographic and mixed layer submesoscale currents in the near-surface southwestern tropical Pacific. *J. Phys. Oceanogr.*, **47 (6)**, 1221–1242.

Srinivasan, K., and W. R. Young, 2014: Reynolds stress and eddy diffusivity of beta-plane shear flows. *J. Atmos. Sci.*, **71**, 2169–2185, doi:10.1175/JAS-D-11-0200.1.

Taylor, S., and D. Straub, 2016: Forced near-inertial motion and dissipation of low-frequency kinetic energy in a wind-driven channel flow. *Journal of Physical Oceanography*, **46 (1)**, 79–93.

Thomas, J., and D. Daniel, 2021: Forward flux and enhanced dissipation of geostrophic balanced energy. *Journal of Fluid Mechanics*, **911**.

Thomas, L. N., 2012: On the effects of frontogenetic strain on symmetric instability and inertia–gravity waves. *Journal of Fluid Mechanics*, **711**, 620–640.

Thomas, L. N., and C. M. Lee, 2005: Intensification of ocean fronts by down-front winds. *J. Phys. Oceanogr.*, **35 (6)**, 1086–1102.

Thomas, L. N., A. Tandon, and A. Mahadevan, 2008: Submesoscale processes and dynamics. *Ocean modeling in an Eddying Regime*, 17–38.

Thomas, L. N., J. R. Taylor, R. Ferrari, and T. M. Joyce, 2013: Symmetric instability in the gulf stream. *Deep Sea Res. Part II: Topical Studies in Oceanography*, **91**, 96–110.

Thompson, A. F., A. Lazar, C. Buckingham, A. C. N. Garabato, G. M. Damerell, and K. J. Heywood, 2016: Open-ocean submesoscale motions: A full seasonal cycle of mixed layer instabilities from gliders. *J. Phys. Oceanogr.*, **46 (4)**, 1285–1307.

Towns, J., and Coauthors, 2014: Xsede: Accelerating scientific discovery. *Computing in Science & Engineering*, **16 (5)**, 62–74, https://doi.org/10.1109/MCSE.2014.80, URL doi.ieeecomputersociety.org/10.1109/MCSE.2014.80.

Wang, S., Z. Jing, Q. Zhang, P. Chang, Z. Chen, H. Liu, and L. Wu, 2019: Ocean eddy energetics in the spectral space as revealed by high-resolution general circulation models. *Journal of Physical Oceanography*, **49 (11)**, 2815–2827.

Wenegrat, J. O., and M. J. McPhaden, 2016: Wind, waves, and fronts: Frictional effects in a generalized ekman model. *Journal of Physical Oceanography*, **46 (2)**, 371–394.

Wenegrat, J. O., L. N. Thomas, J. Gula, and J. C. McWilliams, 2018: Effects of the submesoscale on the potential vorticity budget of ocean mode waters. *Journal of Physical Oceanography*, **48 (9)**, 2141–2165.

Xie, J.-H., and J. Vanneste, 2015: A generalised-lagrangian-mean model of the interactions between near-inertial waves and mean flow. *Journal of Fluid Mechanics*, **774**, 143–169.

Yu, X., A. C. Naveira Garabato, A. P. Martin, D. Gwyn Evans, and Z. Su, 2019: Wind-forced symmetric instability at a transient mid-ocean front. *Geophysical Research Letters*, **46 (20)**, 11 281–11 291.

Zhang, J., Z. Zhang, B. Qiu, X. Zhang, H. Sasaki, W. Zhao, and J. Tian, 2021a: Seasonal modulation of submesoscale kinetic energy in the upper ocean of the northeastern south china sea. *Journal of Geophysical Research: Oceans*, **126 (11)**, e2021JC017 695.

Zhang, Z., X. Zhang, B. Qiu, W. Zhao, C. Zhou, X. Huang, and J. Tian, 2021b: Submesoscale currents in the subtropical upper ocean observed by long-term high-resolution mooring arrays. *Journal of Physical Oceanography*, **51 (1)**, 187–206.